UCSF

Title

Structure-Based Identification of Naphthoquinones and Derivatives as Novel Inhibitors of Main Protease Mpro and Papain-like Protease PLpro of SARS-CoV-2

Authors

Santos, Lucianna H
Kronenberger, Thales
Almeida, Renata G
et al.

Article

Structure-Based Identification of Naphthoquinones and Derivatives as Novel Inhibitors of Main Protease M^pro and Papain-like Protease PL^pro of SARS-CoV-2

Lucianna H. Santos, Thales Kronenberger, Renata G. Almeida, Elany B. Silva, Rafael E. O. Rocha, Joyce C. Oliveira, Luiza V. Barreto, Danielle Skinner, Pavla Fajtová, Miriam A. Giardini, Brendon Woodworth, Conner Bardine, André L. Lourenço, Charles S. Craik, Antti Poso, Larissa M. Podust, James H. McKerrow, Jair L. Siqueira-Neto, Anthony J. O'Donoghue,* Eufrânio N. da Silva Júnior,* and Rafaela S. Ferreira*

Cite This: https://doi.org/10.1021/acs.jcim.2c00693   Read Online

ACCESS | 📊 Metrics & More | 📖 Article Recommendations | 🆘 Supporting Information

ABSTRACT: The worldwide COVID-19 pandemic caused by the coronavirus SARS-CoV-2 urgently demands novel direct antiviral treatments. The main protease (M^pro) and papain-like protease (PL^pro) are attractive drug targets among coronaviruses due to their essential role in processing the polyproteins translated from the viral RNA. In this study, we virtually screened 688 naphthoquinoidal compounds and derivatives against M^pro of SARS-CoV-2. Twenty-four derivatives were selected and evaluated in biochemical assays against M^pro using a novel fluorogenic substrate. In parallel, these compounds were also assayed with SARS-CoV-2 PL^pro. Four compounds inhibited M^pro with half-maximal inhibitory concentration (IC$_{50}$) values between 0.41 μM and 9.0 μM. In addition,

three compounds inhibited PL^pro with IC$_{50}$ ranging from 1.9 μM to 3.3 μM. To verify the specificity of M^pro and PL^pro inhibitors, our experiments included an assessment of common causes of false positives such as aggregation, high compound fluorescence, and inhibition by enzyme oxidation. Altogether, we confirmed novel classes of specific M^pro and PL^pro inhibitors. Molecular dynamics simulations suggest stable binding modes for M^pro inhibitors with frequent interactions with residues in the S1 and S2 pockets of the active site. For two PL^pro inhibitors, interactions occur in the S3 and S4 pockets. In summary, our structure-based computational and biochemical approach identified novel naphthoquinonal scaffolds that can be further explored as SARS-CoV-2 antivirals.
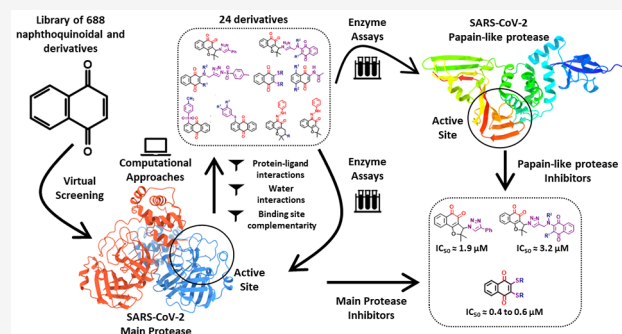
INTRODUCTION

COVID-19 is caused by a β-coronavirus that is related to the virus that was responsible for the severe acute respiratory syndrome (SARS) in 2003 and therefore designated SARS-CoV-2.[1] In December 2019, the first cases of COVID-19 were reported in Wuhan, the capital of Hubei Province, China.[2] The new coronavirus showed a rapid geographical spread, associated with a high infection rate, and the World Health Organization (WHO) declared it as a pandemic in March 2020.[3,4] The rapid transmission from human to human is undoubtedly the main source of contagion, which occurs mainly through droplets, hand contact, or contact with contaminated surfaces.[5] To control the spread of this pandemic virus, biosecurity and hygiene measures are now applied worldwide.[6] Despite the rapid development and emergency authorization of vaccines, viral escape mutants have emerged, and SARS-CoV-2 infections remain a concern for the global community. Therefore, there is a continuing need to discover structural frameworks for drugs that can be employed against COVID-19.[7]

Drug development efforts have targeted the SARS-CoV-2 main protease (M^pro) also known as 3-chymotrypsin-like protease (3CL^pro) or nonstructural protein 5 (nsp5).[8,9] M^pro is an essential cysteine protease that cleaves the precursor replicase polyprotein in a coordinated manner[10] to generate at least 11 nonstructural proteins.[11] As a target, M^pro is conserved among other coronaviruses and has no closely related human homologue.[12−14] Therefore, it has been intensively investigated as a drug target for SARS and Middle East Respiratory Syndrome (MERS).[15−18] M^pro inhibitors with *in vitro* antiviral activity against SARS-CoV-2 have been reported,[19−25] including

Group 1: *Ortho*-quinones

9 compounds

20 compounds   5 compounds   X = Se, 11 compounds   X = S, 5 compounds   7 compounds

4 compounds   6 compounds   9 compounds

Group 2: *Para*-quinones

8 compounds

8 compounds   1 compound   X = O, 9 compounds   X = N, 24 compounds   17 compounds
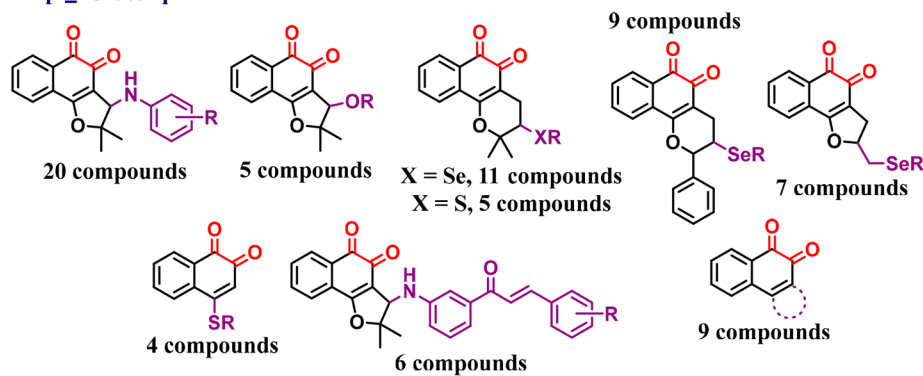
4 compounds   10 compounds
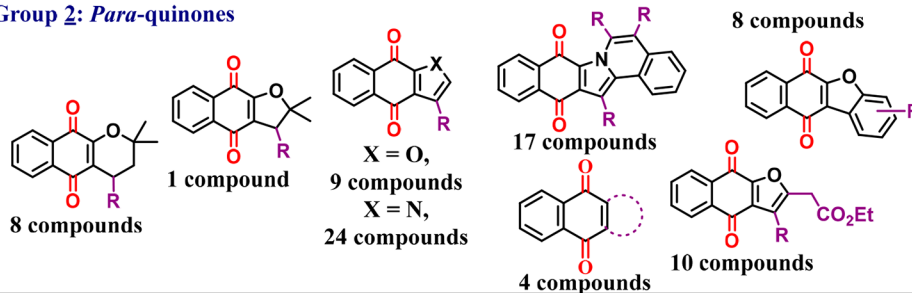
Group 3: *Ortho*-quinone-based 1,2,3-triazoles

16 compounds

44 compounds   21 compounds   2 compounds

1 compound

8 compounds   8 compounds   1 compound   1 compound
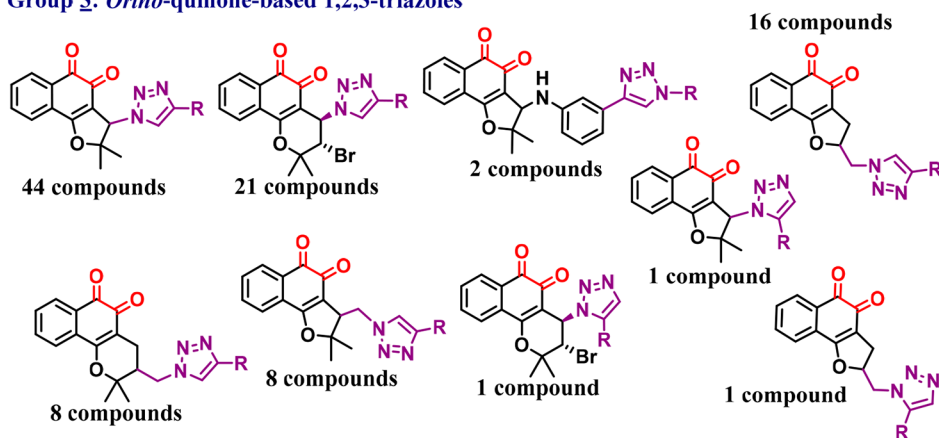
Group 4: *Para*-quinone-based 1,2,3-triazoles

17 compounds

4 compounds   12 compounds

8 compounds   2 compounds   X = N, 30 compounds   X = O, 11 compounds
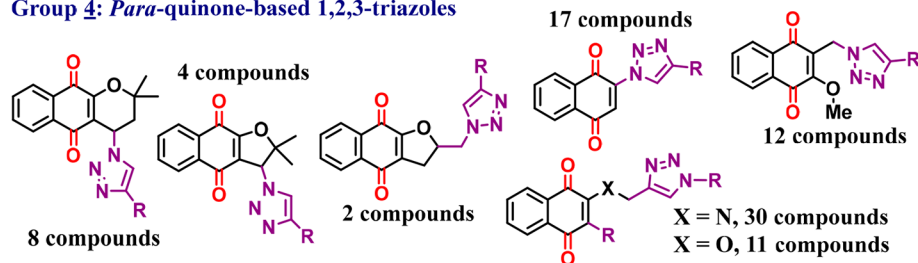
Figure 1. Basic structural framework of the compounds listed in groups 1−4.

peptidomimetic aldehydes,[19,21,23] α-ketoamides,[20,22] calpain inhibitors,[20,23] and nonpeptidic inhibitors.[24−26] Some of these inhibitors binding modes have been determined by crystallography.[20,22−29] Nirmatrelvir, a covalent reversible nitrile, is an orally bioavailable M^pro inhibitor approved for COVID-19 treatment as a combination with ritonavir in the medicine Paxlovid.[30]

Coronaviruses also encode a second cysteine protease, PL^pro, that plays an essential role in the suppression of the host immune system.[31−33] PL^pro cleaves ubiquitin and interferon-stimulated

gene 15 (ISG15) proteins, allowing the virus to evade the host innate immune responses.[10,34] This enzyme can also cleave the viral polypeptide to release the nsp1, nsp2, and nsp3 proteins.[35] SARS-CoV-2 PL^pro inhibitors with antiviral efficacy have been described,[36−39] including naphthalene-based[36−38] and 2-phenylthiophene-based[39] noncovalent compounds, and dozens of crystallographic structures of this protease complexed with a ligand are available.[9,36−41] The crystal structures of M^pro and PL^pro with bound ligands provided us with a structural basis to identify novel inhibitors.
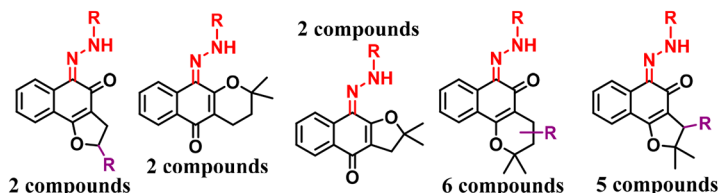
Group 5: phenazine derivatives

12 compounds	9 compounds	5 compounds	2 compounds	5 compounds
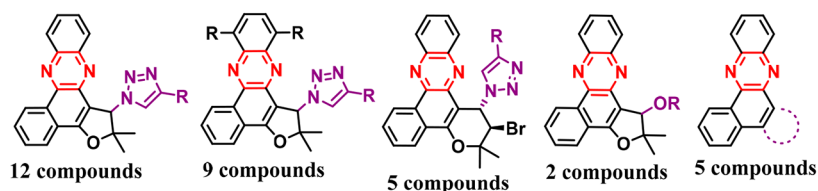
Group 6: 1,4-naphthoquinones and derivatives
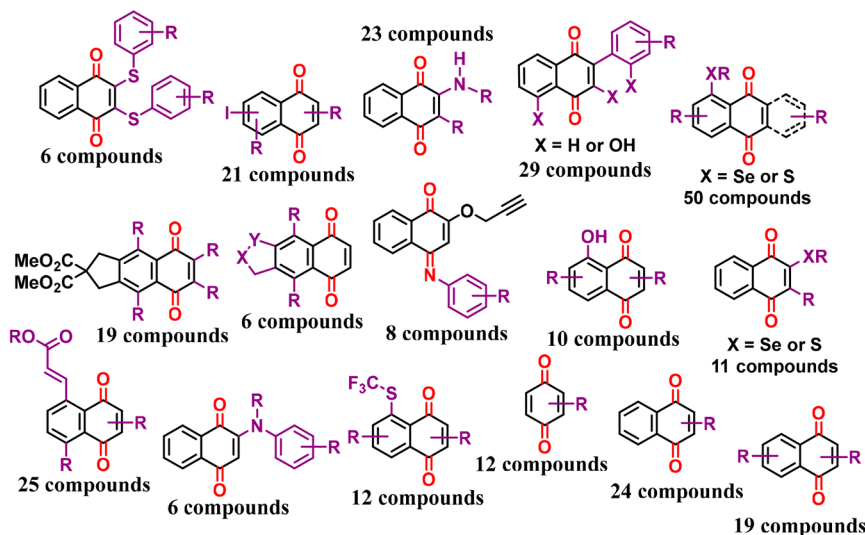
Group 7: hydrazo derivatives
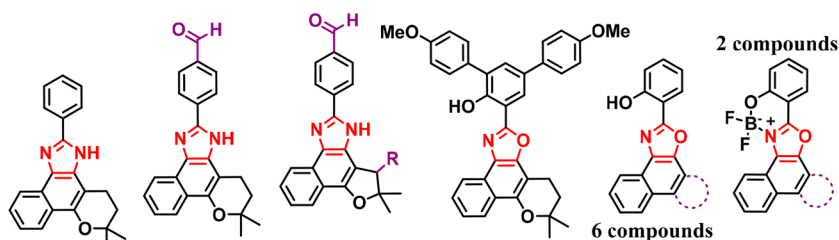

Group 8: Imidazole and oxazole derivatives

Figure 2. Basic structural framework of the compounds listed in groups 5−8.

Repurposing existing chemical libraries is a promising strategy to discover novel therapies.[42,43] Attempts for new therapies for treatment COVID-19 infection are derived from approved drugs, clinical candidates, and other pharmacologically active compounds that were originally developed for other indications.[44−48] For example, remdesivir, a viral RNA-dependent RNA polymerase (RdRp) inhibitor,[49,50] had its emergency use authorization for treatment of hospitalized patients with COVID-19.[51,52] Molnupiravir, another promising heterocycle, has also proven to be effective for oral treatment of COVID-19 in nonhospitalized patients.[53] Despite the recent progress and identification of potential anti COVID-19 drug candidates, the challenge of finding promising drugs remains.

Embelin (Supporting Information, Figure S1), a natural product with a quinone core, has antiviral activity against influenza and hepatitis B.[54,55] Recently, it was shown that embelin may inhibit M^pro and therefore has potential to be used as a treatment of SARS-CoV-2.[56] In addition to embelin, other studies showed that molecules containing a quinoid-like framework also had inhibitory activity against SARS-CoV-2 M^pro. These included celastrol, pristimerin, tingenone, and iguesterin.[57] In this context, based on our experience with quinones and their promising inhibitory evidence, we searched for new quinoid-like structures with potential activity against SARS-CoV-2. In this report, we outline an *in silico* screening of a library of 688 quinones and derivatives against SARS-CoV-2
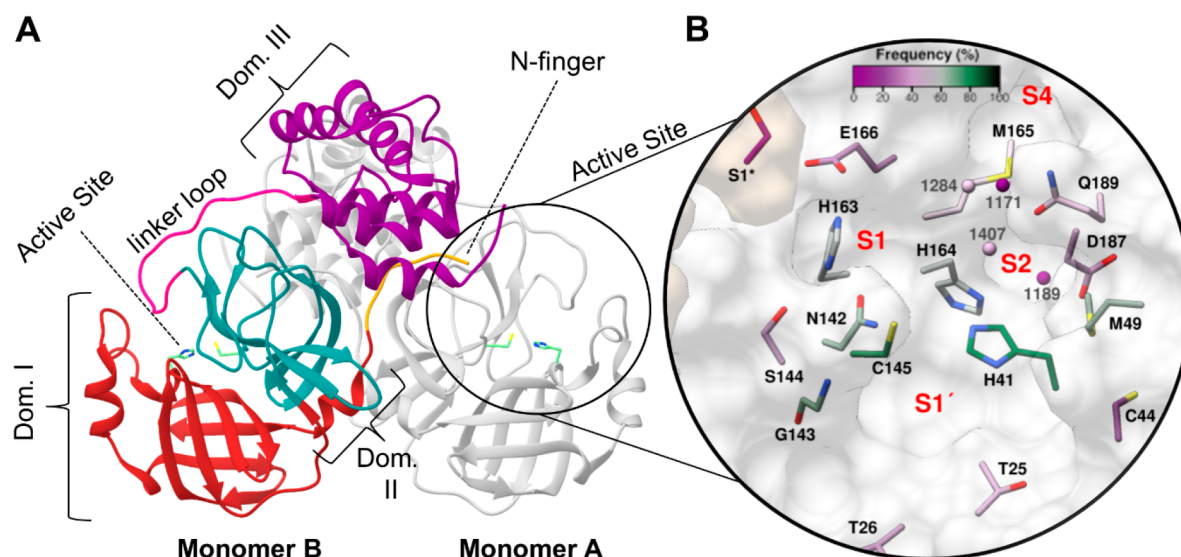
Figure 3. Three-dimensional structure of M^{pro} dimer (PDB code: 5R82[117]) and surface view of the active site. (A) Monomer A is shown in gray, and monomer B is colored according to three domains: red for domain I, blue for domain II, and purple for domain III. The loop linking domains II and III, critical for the protein dimerization, is colored in pink and the N-terminal finger colored orange. (B) Substrate-binding cleft is highlighted with the catalytic residues H$_{41}$ and C$_{145}$ displayed as sticks. In the close-up view of the active site, the residues and conserved water molecules are colored by the frequency they are involved in interactions with 72 crystallography ligands, according to an analysis using the program LUNA.[112]

M^{pro}, from which 24 compounds were selected and tested against this protease.

Based on this strategy, and on experimental screening against PL^{pro} as well, we report novel naphthoquinoidal inhibitors of both SARS-CoV-2 proteases. In addition to biochemical validation, molecular dynamics (MD) simulations indicated the stability of the M^{pro} and PL^{pro} quinoid complexes binding modes, mediated by interactions that were also frequently found in crystallographic complexes of the proteases. These quinones are promising COVID-19 drug candidates to be further explored while also offering valuable insights into M^{pro} and PL^{pro} inhibition.

■ RESULTS

Assembly of a Chemical Library for Virtual Screening against M^{pro}. To search for potential M^{pro} inhibitors, we retrieved a library of quinones and their derivatives, as detailed in Figures 1 and 2 (see Supporting Information, Figures S2−S41, for more structural information). Six-hundred eighty-eight compounds were considered for virtual screening by molecular docking. We divided the molecules into eight different groups as described in Figure 1 (Groups 1−4) and Figure 2 (Groups 5− 8). The compounds listed in Group 1 are ortho-quinones with different substitution patterns. In general, we evaluated compounds containing arylamino,[58−63] alcohol[59] and alkoxy groups,[60,61] selenium and sulfur,[64−66] the basic chalcone framework,[67] among simple ortho-quinones.[60,67−70]

Group 2 is composed of para-quinones. We studied compounds such as α-lapachones,[59,71] arylamino derivatives,[59,63,70] furanonaphthoquinones,[72−74] and pyrrolonaphthoquinones,[72,75] in addition to other derivatives based on para-quinones.[63,74] The selected compounds for this group exhibit a broad substitution pattern but, in general, arylamino and aryl groups are often observed. Compounds with antiviral activity containing the para-quinone core are frequently described in the literature.[76−78]

Groups 3 and 4 consist of ortho- and para-quinones with a 1,2,3-triazole nucleus. Lapachone-based 1,2,3-triazoles have

been studied because of their broad spectrum of biological activities. We studied compounds with aromatic and aliphatic substituents,[60,70,79−85] the presence of selenium,[63,86] BODIPY,[87,88] and sugars,[70] among other substituent groups in the present quinoid structure.[44,89−92]

The phenazine forms of the triazole compounds and quinones described in groups 1 and 3 were also evaluated in group 5.[93−96] Group 6 is the most complete and diverse group addressed in this study, containing approximately two-hundred 1,4-naphthoquinones with broad substitution patterns in the benzenoid A-ring and B-ring. Compounds containing sulfur, as sulfoxides and sulfones,[97,98] selenium,[99] iodine,[46] amines, bromine, hydroxyls, alkenes, among other substituent groups,[45,100−106] were studied and evaluated according to their potential to act as anti-SARS-CoV-2. Imine derivatives were also included in group 6.[66]

Finally, groups 7 and 8 are formed by hydrazo, imidazole, and oxazole derivatives.[107−110] The compounds in these groups were prepared from the quinones described above and represent our attempt to study quinone-derived heterocyclic compounds with biological activity against various microorganisms and their effectiveness against the virus that causes COVID-19.

Available M^{pro} Structures Show Conserved Conformation, Protein−Ligand Interactions, and Location of Water Molecules. As an initial investigation to support the virtual screening of the quinoidal library, we analyzed 72 M^{pro} structures with bound ligands that have a resolution of 1.3 Å to 2.5 Å. Active M^{pro} forms a homodimer comprising two monomers,[19] while its monomer is inactive.[111] Each monomer is formed by domains I, II, and III, binding to each other by an N-terminal finger between domains II and III[24] (Figure 3A). The substrate-binding site is located in a cleft between domains I and II and covered by a loop connecting them. Also crucial to the formation of the active dimer, the N-terminal finger of one monomer extends to the other monomer, shaping and forming the active substrate-binding site.[22] The substrate-binding cleft is composed of four subsites, S1′, S1, S2, and S4,[14,19] which features a noncanonical Cys-His catalytic dyad[19,24] (Figure 3B).

Using principal component analysis (PCA) to assess conformational differences among the structures, we found a high similarity among the M^{pro} structures evaluated (Supporting Information Figure S42A/B). Even for the four most divergent structures (PDB codes: 6M2N,[113] 6W63,[114] 6LU7,[24] and 7BQY,[24] and Supporting Information Figure S42A), carbon alpha ($C\alpha$) root−mean−square deviation (RMSD) between the protease structures is less than 1.0 Å (Supporting Information Figure S42B), suggesting high overall conservation of the quaternary structure.

On the other hand, the M^{pro} active site is known for its high flexibility with conformational changes induced by ligand binding.[24,115,116] Thus, to evaluate possible differences in active site residue conformations, we superimposed six high-resolution M^{pro} structures (1.31 Å to 1.51 Å, PDB codes: 5R82, 5RFW, 5RF6, 5RFE, 5RFV, and 5RF3)[117] with the four structures that were discovered to have lower structural similarity by PCA and had resolutions between 2.10 and 2.20 Å. The superposition of these structures reveals that most residues in the ligand-binding site adopt similar conformations (Supporting Information Figure S43), except for M_{49}, N_{142}, M_{165}, and Q_{189}, which were the most flexible among the other binding site residues.

To better understand the molecular recognition between M^{pro} and inhibitors, we assessed the common protein−ligand interactions found in the 72 experimentally determined crystal structures, of which 49 displayed covalent and 23 noncovalent ligands, using the program LUNA.[112] Within this set, ligands interacted most frequently with the catalytic dyad and residues in the S1 and S2 pockets (Figure 3B). For the catalytic dyad, C_{145} interacts with 78% of the ligands, forming hydrophobic and hydrogen bond interactions, while H_{41} binds to 82% of the inhibitors, mostly through aromatic stacking, hydrophobic, cation−π, and weak hydrogen bond interactions (Figures 3B and 4A). Within the S1 pocket, polar protein−ligand interactions were enriched such as hydrogen bonds and hydrophobic interactions with G_{143} (68% interaction frequency); hydrophobic interactions and weak hydrogen bonds with N_{142} (65% interaction frequency); and cation-nucleophile, cation−π, and hydrogen bond interactions with H_{163} (58% interaction frequency). S_{144} (35%) and E_{166} (29%) in the S1 pocket and D_{187} (33%) and C_{44} (21%) in S2 had lower frequency of interactions (Figures 3B and 4A). On the other hand, the S2 subsite is more hydrophobic. The two residues with the highest interaction frequencies from this pocket were M_{49} (65%) and H_{164} (58%), which formed hydrophobic and weak hydrogen bond interactions, while M_{165} (47%) and Q_{189} (43%) interacted mainly by hydrophobic contacts with the ligands (Figures 3B and 4A). The high frequency of interactions with S1 and S2 residues showed that most of the ligands fill one or both pockets, conserving a more polar profile for S1, whereas the S2 retained a more aromatic and aliphatic profile as observed previously with the SARS-CoV M^{pro}[118] and in other studies with SARS-CoV-2 M^{pro}.[119,120]

Additionally, two S1′ residues, T_{25} (39%) and T_{26} (35%), displayed frequent hydrophobic and weak hydrogen bond interactions. Amino acids in more solvent-exposed pockets, such as S1′ residues L_{27} (13%) and T_{24} (3%), and S4 residues retained few or no interactions (Figure 4A). Several of the hydrogen bond interactions found by LUNA[112] were mediated by water, meaning ligand and protein residues were bridged by a solvent molecule. In M^{pro}, water molecules contribute to ligand stabilization by forming water-mediated hydrogen bonds[19,20,24] and act as a possible third element to the catalytic
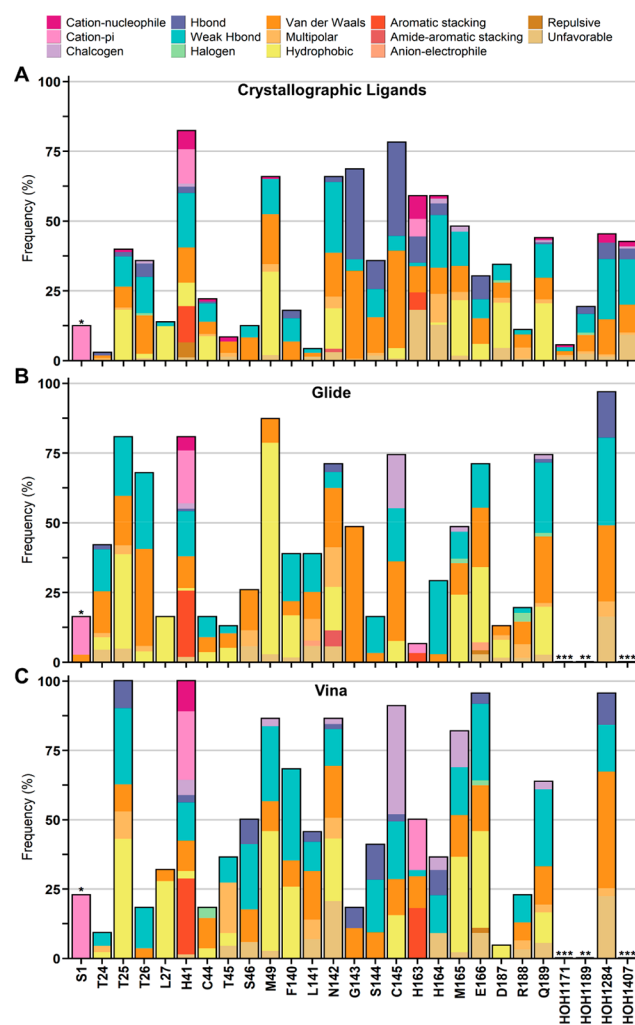

Figure 4. Interaction analysis between M^{pro} binding site residues and ligands from crystallographic structures and docking with Glide and Vina. (A) Frequency and interaction types between residues and 72 crystallographic ligands, the final 24 selected compounds for biochemical assays from both (B) Glide and (C) Vina. Residues with (∗) are from the other monomer. From docking results, the (∗∗) highlight water molecules with no interactions, while (∗∗∗) are water molecules that were not considered in the docking calculations.

dyad.[8,121,122] Therefore, we investigated which water molecules are conserved among the chosen M^{pro} structures using the ProBiS H2O plugin.[123] We found four conserved water molecules (present in over 50% of the structures, Figure 3 and Supporting Information Table S1) that interacted with 20−45% of the ligands, displaying van der Waals, hydrogen bond, and weak hydrogen bond interactions (Figure 4A). Thus, these crystallographic conserved and buried water molecules might be important for ligand recognition.

Virtual Screening of Naphthoquinoidal Compounds against SARS-CoV-2 M^{pro}. Considering the high conservation within the M^{pro} crystal structure conformations, we performed initial molecular docking experiments with the highest-resolution structure (1.31 Å, PDB code: 5R82)[117] from the most populated of the structural clusters, followed by a second round of flexible docking with compounds prioritized from rigid docking. Due to the importance of water molecules in the ligand binding site, we retained two of the four conserved water molecules, that may mediate hydrogen bonds with H_{41}, C_{145},

E_{166}, and L_{167}, for molecular docking (Figure 4A and Supporting Information Table S1). To account for the possibility of water displacement by ligands, a second M^{pro} preparation was also performed in the absence of water molecules. Both preparations were submitted to two distinct docking algorithms, Glide[124] and Autodock Vina.[125]

Docking results were visually inspected and relevant poses were selected according to their overall binding site complementarity and specific protein−ligand interactions. Thus, we prioritized 70 compounds that interacted with the previously established high frequent residues, H_{41}, M_{49}, N_{142}, G_{143}, C_{145}, M_{165}, Q_{189}, and water molecules for flexible docking approaches. Overall, Glide and Vina docking modes established contacts with S1′, S1, and S2 residues. However, a slight shift in interaction patterns was found. Compounds from the quinoidal library did not establish as many hydrogen bond interactions as the crystallographic ligands, giving a more hydrophobic nature to the interactions (Figure 4B/C and Supporting Information Figure S44).

In the second round of docking, we treated M_{49}, N_{142}, M_{165}, and E_{189} as flexible residues, as these were most flexible within crystal structures analyzed and interacted with a high number of ligands (40−65%). Based on these results, we selected 24 (out of 70) compounds that matched the desired residue interactions (Figure 4B/C) and maintained good complementarity to the binding site (Supporting Information Figures S45−S48) for experimental validation in biochemical assays. The compounds selected represent diverse scaffolds from our library, comprising ortho-quinone-based 1,2,3 triazoles (group 3), para-quinone-based 1,2,3 triazoles (group 4), 1,4-naphthoquinones (group 6), and hydrazo derivatives (group 7).

Design and Validation of M^{pro} Substrate. Prior to biochemically evaluating the compounds against M^{pro}, we designed a fluorescent-quenched peptide substrate with the sequence ATLQAIAS that corresponds to the P4 to P4′ amino acids of the nsp7 nsp8 cleavage site. While the AVLQSGFR SARS-CoV 1 M^{pro} substrate is frequently used to measure the activity of SARS-CoV 2 M^{pro}, our substrate sequence was chosen because it most closely matched the consensus sequence for all 11 viral polypeptide cleavage sites (Figure 5A/B).[126] ATL-QAIAS was flanked by 7-methoxycoumarin-4-acetyl-L-lysine on the N-terminus, and dinitrophenyl-L-lysine on the C-terminus. The peptide contains several nonpolar amino acid residues, and therefore, two D-arginine residues were added on the N-terminus to increase solubility. Using a concentration range of 3 μM to 250 μM, the K_M for this substrate was calculated to be 52.1 $\mu M \pm 14.4$ μM (Supporting Information Figure S49A).

Validation of Novel M^{pro} Inhibitors. We evaluated the 24 hit compounds from our virtual screen in a biochemical assay using recombinant SARS-CoV-2 M^{pro}. The enzyme was preincubated with each compound at 10 μM and then assayed with the fluorogenic peptide substrate. To avoid detecting aggregators as false positives,[127,128] our assay was performed in the presence of 0.01% Tween 20. Additionally, we evaluated the absorbance of MCA fluorescence by the compounds to make sure the observed enzyme inhibition was not an artifact of fluorescence, another common cause of false positives in enzyme assays.[129] From this screen, three compounds, one being ortho-quinone-based 1,2,3 triazole (group 3, **191**) and two 1,4-naphthoquinones derivatives (group 6, **379** and **382**), fully inhibited M^{pro}, while two other molecules also from groups 3 and 6, **194** and **415**, respectively, had 50% or more inhibition. **668** was insoluble in assay buffer and was therefore eliminated
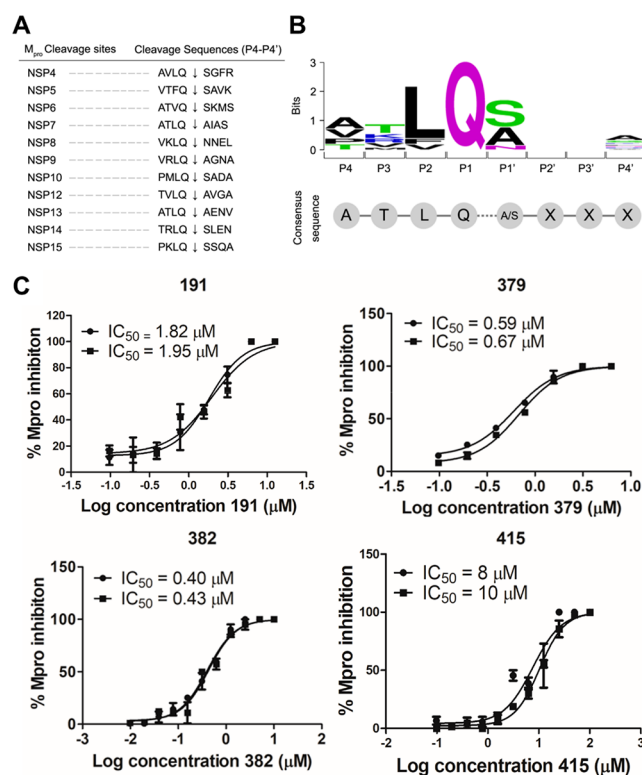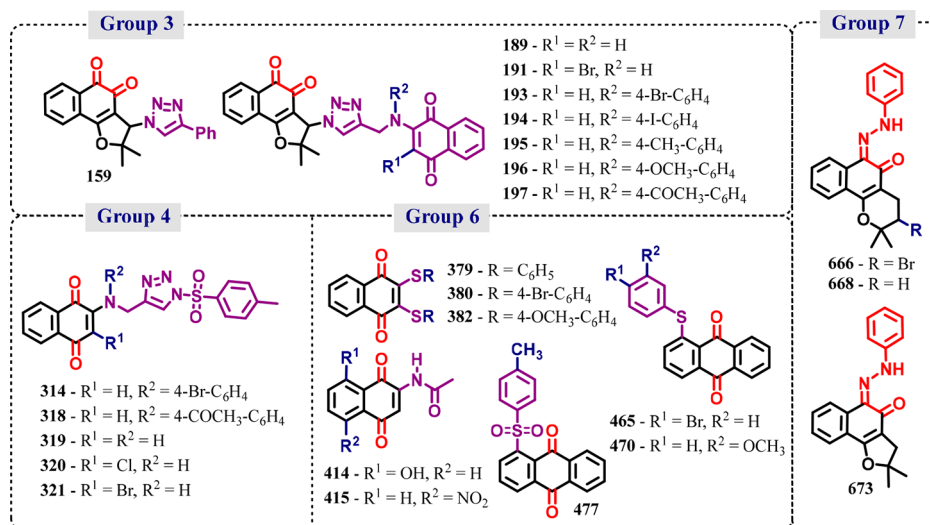

Figure 5. Validation of SARS-CoV-2 M^{pro} inhibitors in enzyme assays. (A) List of the 11 M^{pro} cleavage sites and (B) design of a fluorescent-quenched peptide substrate. The ATLQAIAS substrate was chosen since it closely matches the consensus sequence of all 11 viral polypeptide cleavage sites. (C) IC_{50} curves for SARS-CoV-2 M^{pro} inhibitors. For each compound, two IC_{50} curves are shown, corresponding to two independent experiments (data shown as spheres or squares for each experiment), in which the compounds were preincubated with M^{pro} prior to substrate addition. Each curve was determined based on at least 7 compound concentrations in triplicate.

from further analysis, while the remaining compounds had inhibition profiles of less than 50% (Table 1). The most potent compounds were subsequently evaluated at a concentration range of 100 μM to 9.7 nM and the half-maximal inhibitory concentration (IC_{50}) was calculated to be 1.9 $\mu M \pm 0.06$ for **191**, an ortho-quinone-based 1,2,3 triazole, 9 $\mu M \pm 1$ for **415**, 0.63 $\mu M \pm 0.04$ for **379**, and 0.41 $\mu M \pm 0.015$ for **382** (Table 1 and Figure 5).

To better understand the mechanism of M^{pro} inhibition by naphthoquinone-based derivatives, we evaluated whether compounds **191**, **382**, and **415** were time-dependent inhibitors, a hallmark of covalent-acting molecules. First, enzyme inhibition after 15 min preincubation with the compounds was compared to activity without preincubation.[130] The IC_{50} values observed in these two assay conditions were similar, with slightly lower IC_{50} values upon preincubation (1.9 $\mu M \pm 0.06$ upon incubation vs 5.5 $\mu M \pm 0.5$ without incubation for **191**, 0.42 $\mu M \pm 0.02$ upon incubation vs 0.80 $\mu M \pm 0.06$ without incubation for **382**, and 9.0 $\mu M \pm 1$ upon incubation vs 16 $\mu M \pm 1$ without incubation for **415**) (Figure 6A/B), while for the positive control **GC373** the IC_{50} was 10-fold lower upon preincubation (0.003 $\mu M \pm 0.001$). A dilution experiment was also performed to check whether the compounds were irreversible inhibitors. We incubated the inhibitors and M^{pro} at high concentrations and then diluted the incubation mixture, resulting in inhibitor concentrations 10-fold lower than their apparent IC_{50}. In this

F

Table 1. Percentage of Inhibition at 10 μM and IC$_{50}$ for Naphtoquinoidal Compounds against SARS-CoV-2 M^{pro} and PL^{pro}

	M^{pro}		PL^{pro}	
compound[a]	% inhibition at 10 μM[b]	IC$_{50}$ (μM)[c]	% inhibition at 10 μM[b]	IC$_{50}$ (μM)[c]
159	35 ± 1	ND	100 ± 1	1.90 ± 0.08
189	25 ± 2	ND	100 ± 0	3.25 ± 0.32
191	100 ± 0	1.9 ± 0.06	93 ± 0.7	3.1 ± 0.9
193	32 ± 1	ND	20 ± 4	ND
194	50 ± 7	ND	19 ± 3	ND
195	40 ± 2	ND	25 ± 4	ND
196	29 ± 2	ND	32 ± 2	ND
197	18 ± 4	ND	29 ± 3	ND
314	36 ± 2	ND	55 ± 7	ND
318	45 ± 13	ND	9 ± 5	ND
319	5 ± 2	ND	69 ± 3	ND
320	11 ± 6	ND	31 ± 6	ND
321	40 ± 8	ND	17 ± 0.2	ND
379	100 ± 0	0.63 ± 0.04	0 ± 0	ND
380	12 ± 3	ND	12 ± 6	ND
382	100 ± 0	0.41 ± 0.02	0 ± 0	ND
414	29 ± 2	ND	38 ± 2	ND
415	55 ± 6	9 ± 1	63 ± 9	ND
465	3 ± 5	ND	0 ± 0	ND
470	1 ± 2	ND	6 ± 0	ND
477	5 ± 2	ND	0 ± 0	ND
666	5 ± 5	ND	0 ± 0	ND
668	NT	NT	NT	NT
673	8 ± 3	ND	4 ± 4	ND
GC373	100 ± 0	0.00275 ± 0.0008	NT	NT

[a]See Supporting Information for all structures. [b]Percentages of inhibition are reported as averages and standard deviation of the mean calculated from one experiment performed in triplicate. Compounds were preincubated with enzymes for 15 min before addition of the substrate. [c]IC$_{50}$ values are reported as the averages and standard deviation of the mean, based on two independent experiments. Each IC$_{50}$ curve was determined based on at least 7 compound concentrations in triplicate. ND: not determined. NT: not tested.

assay, an irreversible inhibitor will maintain approximately 10% of enzymatic activity, while a rapidly reversible inhibitor will dissociate from the enzyme to restore approximately 90% of enzymatic activity following the dilution event.[130,131] When this was performed with M^{pro} and **GC373**, a covalent M^{pro} inhibitor (Supporting Information Figure S50), the enzyme remained inhibited upon dilution. The same behavior was observed for compounds **191** and **415** suggesting that these inhibitors are irreversible covalent inhibitors. However, when the same test was carried out with compound **382** enzyme activity returned

after dilution (Figure 6C), indicating that **382** is a reversible inhibitor.

To evaluate the possibility of nonspecific enzyme inhibition through oxidation of the active site Cys, as reported for other M^{pro} quinone inhibitors,[132] we evaluated the effect of adding DTT to the assay buffer upon M^{pro} inhibition. While the addition of DTT reduced inhibition by compounds **191**, **382**, and **415**, the magnitude of this effect was different depending on the compound (Supporting Information Table S2). For **191** and **415**, the presence of 1 mM almost abolished M^{pro} inhibition. Together with the irreversibility observed by these compounds,
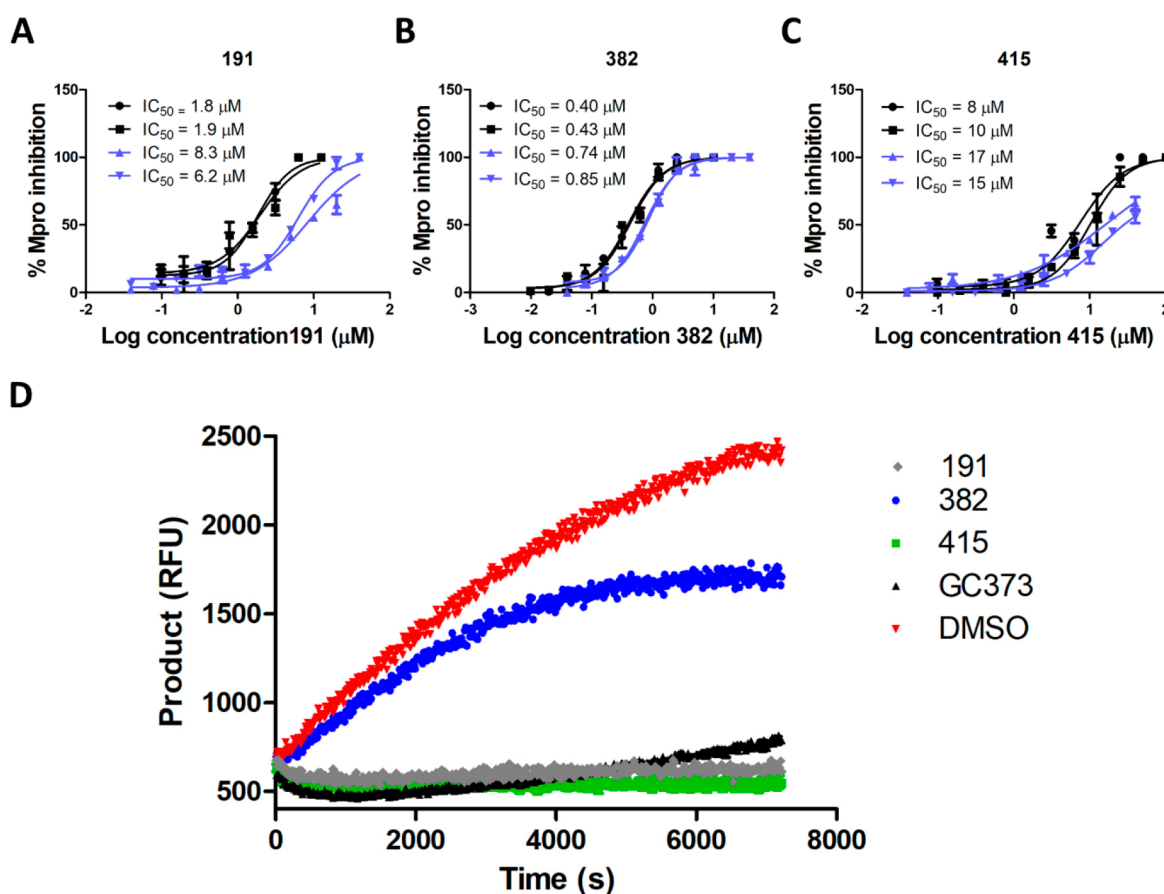
Figure 6. Evaluation of time-dependence and reversibility of M^pro inhibition by compounds **191**, **382**, and **415**. IC_50 curves for SARS-CoV-2 M^pro inhibitors (A) **191**, (B) **382**, and (C) **415**. For each compound, four IC_50 curves are shown, corresponding to two independent experiments in each of the following conditions: compounds preincubated with M^pro prior to substrate addition (black) and without preincubation with the compounds (purple). (D) Reversibility assay. After preincubation of M^pro with compounds, at higher concentrations, the sample was diluted, and product formation was monitored for 120 min. Compound **382** reduced the enzymatic reaction rate by 26% compared to vehicle control (red), while the compounds **191** and **415** reduced product formation by 100%, and this activity was not restored over a 2 h period post dilution, as observed for the covalent inhibitor **GC373** (black).
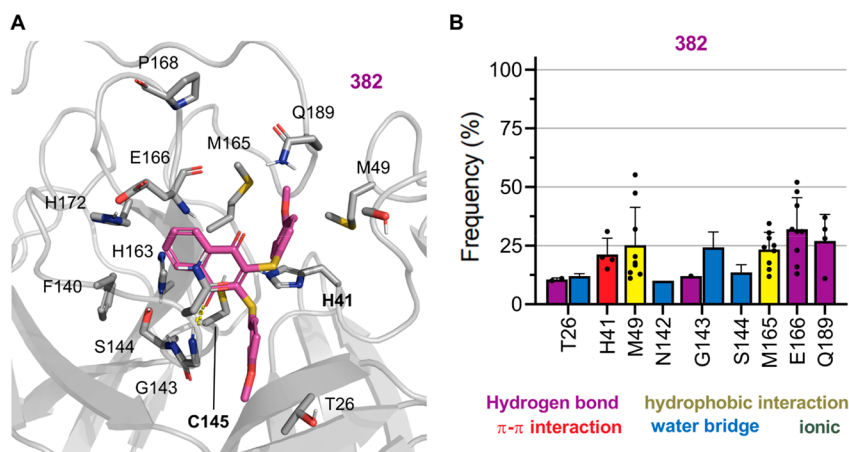

Figure 7. Predicted binding mode of compound **382** to SARS-CoV-2 M^pro. (A) Proposed binding mode from a representative frame in the MD simulation of compound **382** (pink) bound to M^pro, and (B) the frequency of protein−ligand interactions for all simulations. M^pro residues are colored according to the types of atoms in the interacting amino acid residues (protein carbon, light gray; nitrogen, blue; oxygen, red; sulfur, yellow), hydrogen bond interactions are represented as yellow dashed lines. Mean interaction frequency is represented; with standard error of the mean ($N = 5$) interval depicted as error bars, each point displays the individual value for a particular simulation replica and each chain.

these results indicate that **191** and **415** might be nonspecific inhibitors. Further experiments would be necessary to determine its inhibition mechanism. On the other hand, **382**

inhibited M^pro by 40% in the presence of 1 mM DTT and was shown to be a reversible inhibitor in our dilution assays, further validating this compound as a specific M^pro inhibitor.
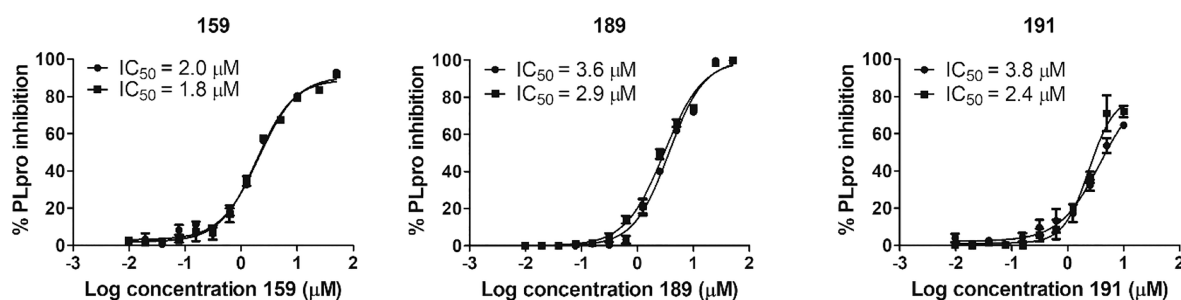
Figure 8. IC$_{50}$ curves for SARS-CoV-2 PL^{pro} inhibitors. For each compound, two IC$_{50}$ curves are shown, corresponding to two independent experiments (data shown as spheres or squares for each experiment). Each curve was determined based on at least 11 compound concentrations in triplicate. Compound **191** was insoluble at concentrations higher than 10 μM.
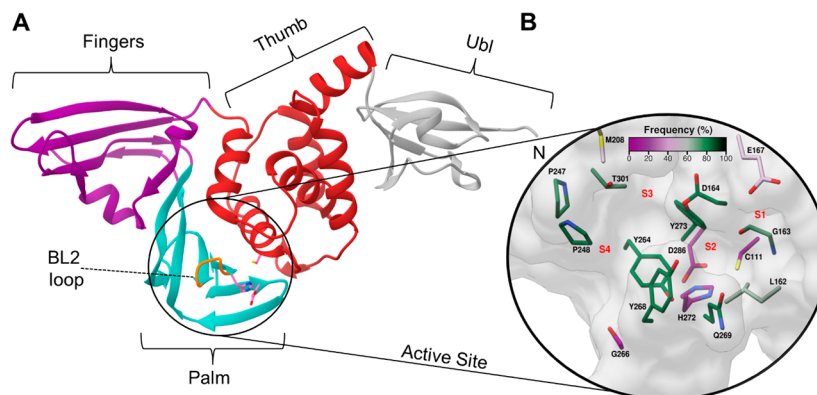

Figure 9. PL^{pro} three-dimensional structure (PDB code: 7LBR)[39] and surface view of the active site. (A) Four domains, fingers (purple), palm (green), thumb (red), and Ubl (gray), are showed in the cartoon representation. The BL2 loop (orange, Gly$_{266}$-Gly$_{271}$) is indicated by a line. (B) Substrate binding cleft is highlighted with the catalytic triad C$_{111}$, H$_{272}$, and D$_{286}$ displayed as sticks (pink). In the close-up view of the active site, the residues are colored by the frequency they are involved in interactions with 21 crystallography ligands, according to an analysis using the program LUNA.[112]

To gain insights into the proposed binding mode of our M^{pro} inhibitors and guide future optimization efforts, we conducted docking and MD studies with compound **382**, a representative from the specific M^{pro} inhibitor scaffold discovered. Our simulations considered **382** to be noncovalently bound to both monomers in the M^{pro} dimer. However, the loss of interactions with E$_{166}$ resulted in ligands being expelled from one of the binding sites within a few nanoseconds (~200 ns) of simulation. Our analysis is focused on the other binding site that retained the ligand with stable interactions along the analyzed trajectory.

The most representative binding mode observed for **382** in the MD simulations (Figure 7A) retains key interactions proposed based on docking with Glide (Supporting Information Figure S46), despite the variability in the ligand orientation, leading to four clusters with frequency between 17.5 and 31.7% (Supporting Information Figure S51). Compound **382** displays stable polar contacts (hydrogen bond and water bridges) with G$_{143}$ and S$_{144}$ in the S1 pocket and π−cation or π−π interactions with the side chain of H$_{41}$. The ligand also displays stable polar interactions with the main-chain nitrogen from E$_{166}$ and electrostatic contacts with its side-chain (Figure 7), a residue that adopts a stable conformation due to an interaction between its side chain and the S1 from the other monomer (S$_1$*). Hydrophobic interactions to M$_{49}$ and M$_{165}$ from the S2 pocket are seldom observed for this inhibitor.

Simulations with compound **415**, an irreversible inhibitor, were also done. In these simulations, **415** was covalently bound to C$_{145}$ retaining stable interactions with key S1′ and S2 subsites residues (Supporting Information Figure S52). Although

compound **415** might be a nonspecific inhibitor, this binding mode may guide novel chemical modifications.

Validation of Novel PL^{pro} Inhibitors. Although our virtual screening studies were focused solely on M^{pro}, we were also interested in testing the virtual screening hits against the second SARS-CoV-2 cysteine protease, PL^{pro}, to determine if any of the molecules were dual inhibitors of the viral enzymes. PL^{pro} cleaves three sites on the viral polypeptide but also acts as a deubiquitinase. Therefore, we identified a fluorogenic substrate for human deubiquitinases (Z-RLRGG-7-amino-4-methylcoumarin) as a substrate for SAR2-CoV-2 PL^{pro}. Recombinant PL^{pro} was incubated with 6 μM to 500 μM of this substrate, and the K_M value was calculated to be 376.6 ± 32.3 μM (Supporting Information Figure S49B). PL^{pro} enzyme was preincubated with the same set of 23 compounds at 10 μM, in the presence of 0.01% Tween-20 and 0.1 mM DTT, and then assayed with the fluorogenic substrate. Compound **668** was again eliminated due to insolubility in the assay buffer. Surprisingly, a total of 12 compounds inhibited PL^{pro} by >50% and the top three (compounds **159**, **189**, and **191**) inhibited at >90%. These top compounds are ortho-quinone-based 1,2,3-triazoles derivatives, sharing a common scaffold. The IC$_{50}$ values were calculated to be 1.9 μM, 3.2 μM, and 3.1 μM for compounds **159**, **189**, and **191**, respectively (Figure 8). Enzyme inhibition by these compounds was not sensitive to the DTT concentration (Supporting Information Figure S53). Among the compounds that caused lower PL^{pro} inhibition, five are N-substituted analogs of these hits, compounds **193−197**. Due to solubility limitations and their weaker potency, it was not possible to obtain reliable IC$_{50}$ values for compounds **193−197**.
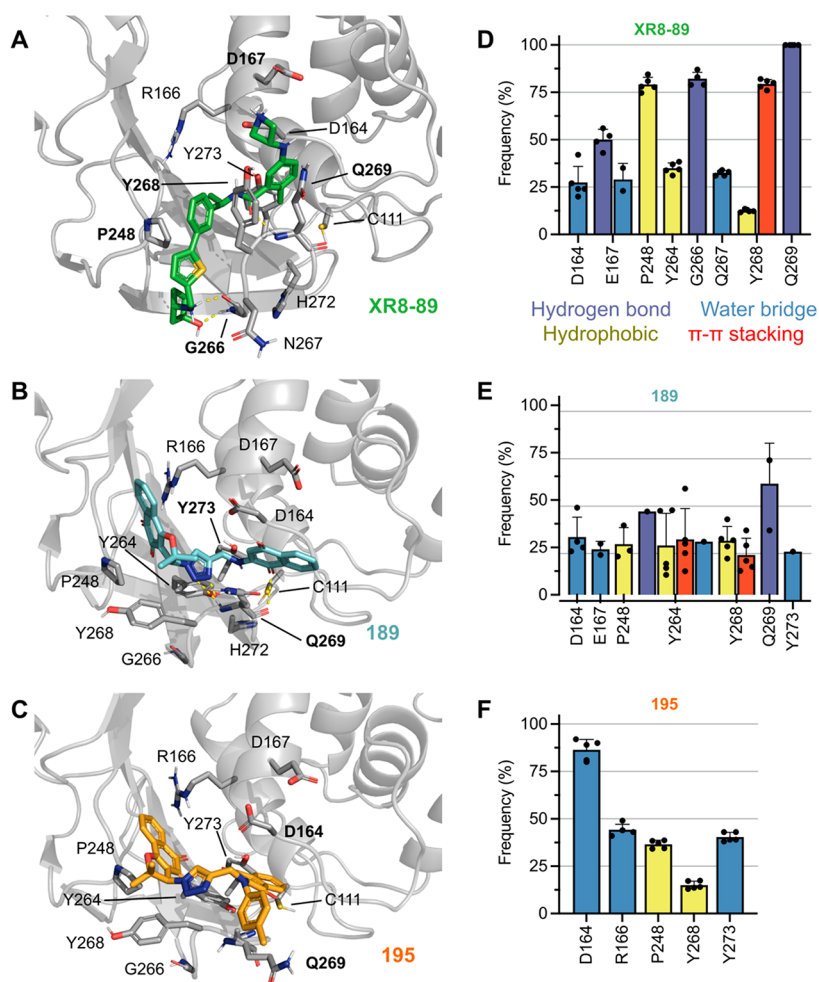
Figure 10. Proposed binding modes and protein−ligand interactions profile for PL^{pro} inhibitors. (A−C) Representative frames from the MD simulation describing the potential binding mode for compounds XR8-89 (green, from PDB code: 7LBR),[39] **189** (cyan), and **195** (orange) bound to PL^{pro}. PL^{pro} residues are colored according to the types of atoms in the interacting amino acid residues (protein carbon, light gray; nitrogen, blue; oxygen, red; sulfur, yellow), and hydrogen bond interactions are represented as yellow dashed lines. Frequency of protein−ligand interactions for all simulations with ligands (D) XR8-89, (E) **189**, and (F) **195**. Mean interaction frequency is represented, with standard error of the mean (N = 5) interval depicted as error bars; each point displays the individual value for a particular simulation replica.

These eight PL^{pro} inhibitors share a tricyclic 1,2-naphthoquinone ring that seems important for enzyme inhibition, as its replacement by a para-tolyl sulfone abolished activity against PL^{pro} (compare compounds **189** vs **319**; **191** vs **321**; Table 1).

Since the PL^{pro} inhibitors have a shared scaffold, we selected compounds **189** and **195** (*N*-substituted) for computational studies. The SARS-CoV-2 PL^{pro} has similar folding to the homologous enzymes from other coronaviruses,[133] with domains showing a "thumb-palm-fingers" pattern and an *N*-terminal ubiquitin-like (Ubl) domain (first 60 residues) (Figure 9A).[39] As a cysteine protease, PL^{pro} contains a canonical catalytic triad, Cys-His-Asp (C_{111}, H_{272}, and D_{286})[10] located in a solvent-exposed cleft at the interface of the palm and thumb domains.[39] Analysis of common protein−ligand interactions from the crystallographic structures showed little or no interaction with the catalytic triad, in agreement with very narrow S1 and S2 pockets, which have high specificity for glycine (Figure 9B and Supporting Information Figure S54). Only covalently bound peptidic inhibitors, containing glycines at P1 and P2, occupy these pockets.[36,39] Instead, the noncovalent ligands bind to a groove corresponding to the S3 and S4 subsites, approximately 8 Å from the catalytic cysteine.[36] This groove is created due to the

blocking loop 2 (BL2 loop), a flexible substrate-binding loop (Gly_{266}-Gly_{271}) found adjacent to the active site (Figure 9A/B). The BL2 loop is found in an open conformation in unbound PL^{pro}, while it closes upon substrate or inhibitor binding.[36] As observed for the crystallography ligands, compounds **189** and **195** showed docking predicted binding modes occupying the S3 and S4 subsites (Figures 9, 10, and Supporting Information Figure S54). To verify the stability of these proposed binding modes, compounds **189** and **195**, a N-substituted derivative of **189** less potent against the enzyme, underwent MD simulations. The XR8-89 ligand (PDB code: 7LBR)[39] was used as a positive control (Supporting Information Figure S55).

In simulations with XR8-89, the BL2 loop remained in the closed conformation, and the ligand binding mode remained stable in all simulations, with its core structure being stabilized by hydrogen bond interactions between the carbonyl group and the backbone of Q_{269} (100% of the analyzed simulation time), as well as π-stacking interactions with Y_{268} (79% of the analyzed simulation time) (Figure 10 and Supporting Information Figure S56). We also observed a water bridge between the nitrogen on the amide and D_{164} (subsite S3, present on average 22% of the analyzed trajectory).

J

For **189**, four of the five simulated replicas showed stable interactions, with the initial pose changing dramatically from the initial coordinates after 500 ns in one of the replicas. In terms of binding mode, the triazole and central amine groups of **189** stabilized hydrogen bond interactions with the Q_{269} (35% of the analyzed trajectory) and π-based interactions with Y_{264} and Y_{268}. The carbonyl groups from the naphthalene-1,4-dione moiety displayed water-mediated interactions with D_{164}. The 1,2-naphthoquinone ring, shown to be essential for protease inhibition in our biochemical assays, binds to the S4 pocket, establishing hydrophobic interactions to P_{248} (Figure 10B).

In contrast to the observed for XR8-89 and **189**, the tolyl substituent on the amine of **195** prevented stable simulations on BL2 closed conformation (Supporting Information Figure S57). Thus, we performed 1 μs simulation initially, which displayed at first few interactions with the side chain of Q_{269} (less than 20% of simulation time) and later stable interactions with D_{164} (over 66% of simulation time) while leading to the opening of BL2 and accommodating of the ligand. The last frame of this simulation was used to generate a further five new replicas (5 × 500 ns), to analyze the stability of this new binding mode, which was shown to be stabilized by water bridges with the D_{164} (>75%), R_{166} (>40%), and Y_{273} (~40%) and hydrophobic contacts with P_{248} (>40%) (Figure 10). Interestingly, the interaction pattern for **195** differed from the observed for ligands XR8-89 and **189**, as hydrogen bond interactions with Q_{269} and π-based interactions with Y_{268} were not observed. The absence of these interactions might be related to the lower potency of **195** against PL^{pro}.

Evaluation of Hit Compounds in a SARS-CoV-2 Viral Infection Assay. We evaluated two M^{pro} hit compounds **382** and **415** and the PL^{pro} hit compounds **189** and **191** in a SARS-CoV-2 viral infection assay of monkey-derived Vero E6 cells. The clinically approved RNA-polymerase inhibitor remdesivir was used as a positive control.

Remdesivir displayed antiviral efficacy in Vero E6 cells with EC_{50} of 2.45 μM and no host cell toxicity at concentrations up to 20 μM. Under the same culture conditions, the hit naphthoquinone compounds were tested in three concentrations (24 μM, 6 μM, and 1.4 μM) and showed no significant antiviral activity dissociated from host cytotoxicity. Since compound **382** did not show antiviral activity at the lowest concentration, it was removed for further evaluations. The remaining compounds were tested in serial dilution starting at 1 μM, both in Vero E6 cells (Supporting Information Figure S58) and in infected human-derived HeLa cells expressing ACE2. For HeLa-ACE2 cells, remdesivir was more potent with EC_{50} of 40 nM; however, cell cytotoxicity was also noted at concentrations above 2.4 μM. At lower concentrations, the naphthoquinone compounds had no significant antiviral activity up to 1 μM (Supporting Information Figure S59). Therefore, it is important to further study the mechanism of action to understand the cytotoxicity and decouple from the direct antiviral activity.

■ DISCUSSION

In this study, we used computational and biochemical approaches to evaluate a library of quinones to find inhibitors against SARS-CoV-2 proteases. The wealth of structural information from M^{pro} and PL^{pro} allowed us to generate patterns of common protein−ligand interactions, which were helpful in two stages of our computational analysis. First, the selection of computational hits was guided by protein−ligand interactions frequently observed in M^{pro} crystallographic complexes. Thus, we prioritized compounds that interacted with conserved water

molecules, S1 and S2 residues, filling one or more of the subsites with minimum solvent exposure. This strategy was successful as, among 24 compounds selected for inhibitory assays, we identified at least one scaffold confirmed as specific M^{pro} inhibitors with submicromolar potency (compounds **382**, IC_{50} of 0.41 μM; **379**, IC_{50} of 0.63 μM). Additionally, for M^{pro} and PL^{pro} inhibitors that were evaluated experimentally, we conducted MD simulations of the protein−ligand complexes. Together with the observed stability of binding poses during the simulations, the fact that our inhibitors establish interaction patterns commonly observed in the crystal structures encourages the application of our results in structure-based optimization projects.

During the validation of M^{pro} and PL^{pro} inhibitors, several precautions were taken to avoid artifactual inhibition. We were especially careful considering previous reports that indicate quinones as potential pan assay interference compounds (PAINS).[134] To avoid common causes of artifacts,[128−130] we conducted the assays in the presence of detergent, avoiding compound aggregation, and verified that compounds were not highly fluorescent. In addition, a comparison of the inhibition of both target enzymes by each of the compounds indicates that the inhibitors showed specificity to one of our targets, reducing the likelihood they would be promiscuous inhibitors. Furthermore, to assess if M^{pro} inhibitors were time-dependent and/or irreversible inhibitors, we determined IC_{50} values of compounds **191**, **382**, and **415** upon or without preincubation with the enzyme and evaluated recovery of enzyme activity in a reversibility assay. Our results indicated that compound **382** is a reversible M^{pro} inhibitor, while **191** and **415** bind irreversibly to the target. Finally, evaluation of the effect of DTT on enzyme inhibition indicated that, while the irreversible inhibitors may be nonspecific oxidative agents, compound **382** represents a specific scaffold of M^{pro} inhibitors. The specificity of this compound is further strengthened as it did not inhibit PL^{pro}.

Our MD simulations of **382** in complex with M^{pro} suggested that stability occurs via multiple intermolecular interactions, with H_{41}, G_{143}, and E_{166}. All three residues have reported key roles in the active site. As part of the catalytic dyad, H_{41} serves as a base for nucleophilic attack performed by C_{145} in peptide-bond cleavage,[135] while G_{143}, an oxyanion hole residue, helps stabilize the tetrahedral intermediate of the peptide-bond cleavage.[136] Moreover, E_{166} is essential for dimerization, and its interactions with the other monomer N-finger also aid the correct orientation of H_{163} and H_{172} to form the S1 pocket.[136,137] However, long-lasting interactions were observed only in the binding site of one monomer, while the ligand bound to the other monomer was expelled within a few nanoseconds. The instability in one of the monomers was observed as a reproducible pattern in most replicates of our MD simulations. The complete deletion of the N-finger (residues $S_1^* − R_4^*$) in SARS-CoV M^{pro} reduces the extent of the dimerization and completely abolishes the enzymatic activity (<1%).[138] Simulations of M^{pro} from SARS-CoV-2 with peptidomimetic inhibitors or substrate[139] suggest that a similar mechanism exists, where the N-finger conformation upon dimerization exerts a direct influence on the oxyanion-loop motions and the stabilization of the catalytic conformation.

Our initial focus was on M^{pro} inhibition; however, we also tested the 23 soluble compounds selected against PL^{pro} to possibly find dual inhibitors for both SARS-CoV-2 viral enzymes. While we did not characterize dual inhibitors, three *ortho*-quinone-based 1,2,3-triazoles had IC_{50} in the single-digit

micromolar range against PL^{pro} (Compounds **159**, IC$_{50}$ of 1.9 μM; **189**, IC$_{50}$ of 3.2 μM; and **191**, IC$_{50}$ of 3.1 μM). Considering the evidence supporting each SARS-CoV-2 protease as a therapeutic target,[36,140,141] these compounds are interesting even in the absence of dual inhibition.

MD simulations of **189** and **195** bound to PL^{pro} were not as stable as the positive control XR8-89 (PDB code: 7LBR).[39] The two scaffolds interacted, with low or moderate frequency, with residues in the S3 and S4 subsites. However, differences were observed in the frequency of interactions with key residues such as Y$_{268}$ and Q$_{269}$. These two residues form an unusual β-turn in the flexible β-hairpin BL2 loop that controls the access to the active site in the binding of host and viral proteins.[39] A previous supervised MD study suggested that the interactions between naphthalene-based ligands and residues Y$_{268}$ and Q$_{269}$ are directly responsible for the unbinding process of ligands since they can drag them away as the BL2 loop fluctuates.[142] Their hypothesis is that the BL2 loop natural flexibility is responsible for not only trapping the substrate but also expelling the product, using strong interactions with these two residues to catch the ligand and expose it to the solvent. However, in our recent work with unsupervised MD simulations, we observed that ligand binding was stabilized by interactions with Y$_{268}$ and Q$_{269}$, with the BL2 loop sustaining the closed conformation, combined with the inhibitors' substitutions filling in unique subpockets adjacent to the BL2 loop.[143] Therefore, we suggested that compounds with bulkier substituents that bind among BL2 groove and loop could improve their binding affinity. On the other hand, from our MD simulations, interactions with Y$_{268}$ and Q$_{269}$ had lower frequency in the case of **189** and were not observed for **195**, thus not fully stabilizing the closed conformation of BL2 loop. Although this might explain their lower potency against PL^{pro}, these inhibitors interacted with some interesting and underexplored residues, offering possible information for optimization.

■ CONCLUSIONS

Here we employed computational and biochemical assays to evaluate a quinone library. Based on a detailed experimental characterization, including assessment for aggregator properties, fluorescence, and promiscuous inhibition by oxidation, we identified one promising scaffold of specific naphthoquinone inhibitors against each of the two SARS-CoV-2 viral proteases, M^{pro} and PL^{pro}, with potency in the one-digit micromolar to nanomolar range. We propose likely binding modes for these inhibitors, with good complementarity to the protease active sites, that closely resemble protein−ligand interaction patterns observed in crystallographic complexes and which were stable in MD simulations. Hence, the inhibitors presented here are novel scaffolds for further optimization to develop a treatment against SARS-CoV-2 infection.

■ EXPERIMENTAL SECTION

Compounds General Experimental Details. All chemicals were obtained from commercial sources and used without further purification. Melting points were obtained on a Thomas-Hoover apparatus and uncorrected. Column chromatography was performed on silica gel (Silica Flash G60 UltraPure 60−200 μm, 60 Å). Infrared spectra were recorded on a Shimadzu FTIR Spectrometer IR Prestige-21. ^{1}H and ^{13}C NMR were recorded at room temperature using a Bruker AVANCE DRX 200 and DRX 400 MHz, in the solvents indicated, with tetramethylsilane

(TMS) as internal reference. Chemical shifts (δ) are given in parts per million (ppm) and coupling constants (J) in Hertz (Hz). The mass spectrometer was operated in the positive ion mode. A standard atmospheric pressure photoionization (APPI) source was used to generate the ions. The sample was injected using a constant flow (3 μL/min). The solvent was an acetonitrile/methanol mixture. The APPI-Q-TOF MS instrument was calibrated in the mass range of 50−3000 m/z using an internal calibration standard (low concentration tuning mix solution) supplied by Agilent Technologies. Data were processed employing Bruker Data Analysis software version 4.0. Compounds were named following IUPAC rules as applied by ChemBioDraw Ultra (version 12.0).

Synthesis of Candidate Inhibitors. Ortho-quinone-based 1,2,3-triazoles compounds **159**, **189**, and **191−197** were prepared according to previous reports, and their data are consistent with the literature.[79,81,90,144] Para-quinones-based 1,2,3-triazoles compounds **314** and **318−321** were prepared as described in the literature.[89] Para-quinones and derivatives **379**, **380**, **382**, **414**, **415**, **465**, **470**, and **477** were synthesized following the previously published studies in the literature.[75,98] Hydrazo derivatives **666**, **668**, and **673** were prepared according to previously published reports, and their data are consistent with the literature.[67]

Comparison of Available SARS-CoV-2 M^{pro} Structures. All 72 crystallographic structures were downloaded from the PDB[145] (structures available in April 2020). Structural superposition was performed with program R's package,[146] Bio3D,[147] using the protein's Cα. RMSD and PCA were also done with Bio3D package. As water molecules might play important roles in M^{pro} catalysis and ligand stabilization, we used the ProBiS H2O plugin.[123] This PyMol[148] plugin enables the identification of conserved water sites in proteins using experimental determined protein structures. The highest resolution structure, PDB code 5R82,[117] was used as reference to establish the water molecules position.

Analysis of Protein−Ligand Interactions. The program LUNA[112] was used to perform large-scale analysis of non-covalent interactions between the protein−ligands complexes of M^{pro}. With this program, it was possible to identify frequently interacting residues between the ligands and M^{pro} active site. We submitted a list containing the PDB ids of the 72 structures, discriminating chain A and the binding site ligands to be analyzed. After processing, we investigated the table (in .csv format) of the interacting frequencies by residues and ligands with the program R.

Ligand and Protein Preparation. Three-dimensional ligand structures were generated with LigPrep (version 46013), using Epik to predict their protonation in pH 7.0 ± 2.0, and generating tautomers and diastereoisomers. The OPLS3e force-field was employed for structure generation. The SARS-CoV-2 M^{pro} protein structure was prepared from the PDB 5R82,[117] using the Protein Wizard Preparation tool, with standard options. Two M^{pro} receptor files were prepared for docking: one with all water removed and another containing waters 1189 and 1284 from the original PDB. The SARS-CoV-2 PL^{pro} structure was prepared from the PDB 7LBR[39] using the same protocol as M^{pro}.

Molecular Docking. Molecular docking was carried out with Glide SP (version 9.1) and Autodock Vina. For docking to M^{pro} with Glide,[124] grids were centered at the central point of the active site residues G$_{143}$, C$_{145}$, M$_{49}$, and H$_{41}$ (coordinates: 10.7313390385, −4.49000171154, 22.4985591538). Two

docking grids were generated: one without waters and one containing the two conserved waters described in the protein preparation. Each compound was docked using both grids. In both cases, the dimensions of the inner box had 10 Å in each direction and the outer box had 30 Å in each direction. Whenever mentioned, covalent docking was performed using CovDock[149] using the C_{145} as anchor, nucleophilic addition to double bond as reaction type, and generating up to 10 poses for each ligand. Poses were selected according to the docking score and relevant interactions.

For docking to M[pro] with Autodock Vina,[125] a grid box of size $22.5 \times 24.5 \times 22.5$ Å^3 was centralized in the geometrical center among the residues T_{26}, M_{49}, N_{142}, and M_{165}. All the experiments were done in triplicate starting from a random seed. Energy range, exhaustiveness, and the number of maximum modes parameters were set to 3 kcal/mol, 8, and 9, respectively. Similar to docking using Glide, two experiments were done with and without conserved waters. For selected ligands, induced-fit docking was performed (with and without the conserved waters) by flexing the residues N_{142}, E_{189}, M_{49}, and M_{165}.

For docking to PL[pro], only Glide was used: using the Induced-Fit mode,[150] a cubic grid box of size 12 Å was centralized in the geometric center of the cocrystallized ligand (PDB code: 7LBR).[39]

Redocking of the crystallographic ligands from M[pro] and PL[pro] (PDB codes: 5R82 and 7LBR, respectively) was successfully performed (RMSD ≤ 2.0 Å) to validate the docking protocol used here (Supporting Information Figure S60).

Molecular Dynamics Simulations. Prepared SARS-CoV-2 M[pro] and PL[pro] structures were simulated with the selected ligands. MD simulations were carried out by using the Desmond engine[151] with the OPLS3e force-field[152] according to a previously described protocol.[153] In short, the system encompassed the protein−ligand/cofactor complex, a predefined water model (TIP3P)[154] as a solvent and counterions (Na$^+$ or Cl$^-$ adjusted to neutralize the overall system charge). The system was treated in a cubic box with a periodic boundary condition (PBC) specifying the shape and the size of the box as 13 Å distance from the box edges to any atom of the protein. Short-range Coulombic interactions were calculated using 1 fs time steps and 9.0 Å cutoff value, whereas long-range Coulombic interactions were estimated using the smooth particle mesh ewald (PME) method.[155] Each M[pro] and PL[pro] system was subjected to at least 5 μs simulations (five replicas of 1 μs each), with exception of PL[pro], compound **195**, which had one preliminary 1 μs simulation, from which a stable conformation was selected for further shorter simulations. Atomic interactions and distances were determined using the Simulation Event Analysis pipeline as implemented in Maestro 2021.2 (Schrödinger LCC).

Representative frames of the simulations were retrieved from clustering, which was performed with hierarchical clustering analyses. Trajectories were clustered using the script trj_cluster.py (implemented in Maestro 2021.2, Schrödinger LCC) using 2 Å as cutoff, which was chosen upon evaluating the RMSD of ligand's heavy atoms. Trajectories where the ligand was expelled of the pocket were not considered for clustering or interaction analyses.

RMSD values of the protein backbone were used to monitor simulation equilibration and protein folding changes. MD trajectories were visualized and figures produced by PyMol v.2.4 (Schrödinger LCC, New York, NY, USA).

Synthesis of M[pro] Substrate. A quenched fluorogenic peptide substrate with the sequence (D-Arg)-(D-Arg)-Lys-(MCA)-Ala-Thr-Leu-Gln-Ala-Ile-Ala-Ser-Lys(DNP)-COOH (ATLQAIAS) was synthesized on a Biotage Syroll peptide synthesizer at room temperature through fluorenylmethyl-oxycarbonyl (Fmoc) solid-phase synthesis. The synthesis scale was 12.5 μmole with preloaded lysine(2-dinitrophenyl) Wang resin, where the DNP quencher was linked to the epsilon nitrogen of the lysine. For each coupling reaction, 4.9 equiv of HCTU (O-(1H-6-chlorobenzotriazole-1-yl)-1,1,3,3-tetramethyluronium hexafluoro-phosphate), 5 equiv of Fmoc-amino acid−OH, and 20 equiv of N-methylmorpholine (NMM) in 500 μL of N,N-dimethylformamide (DMF) were used. The coupling reaction was carried out with shaking for 8 min. Each amino acid position was double coupled, and subsequent Fmoc deprotection was done with 500 μL of 40% 4-methylpiperidine in DMF for 10 min. Deprotection was followed by a wash with 500 μL of DMF for 3 min and the wash was repeated 6 times. The lysine amino acid, lysine (7-methoxycoumarin-4-acetic acid (MCA), was coupled where MCA was linked to the epsilon nitrogen of the lysine. The two final amino acid position couplings used D-arginine to increase peptide solubility. The cleavage of the peptide from the Wang resin was carried out with a 500 μL of solution composed of 95% trifluoroacetic acid, 2.5% water, and 2.5% triisopropylsilane at room temperature for 1 h with shaking. The crude peptide product was precipitated in 30 mL of a 1:1 mixture of cold diethyl ether and hexane. Product was then solubilized in a 1:1:1 mixture of DMSO, water, and acetonitrile. The solubilized crude material was purified by high-performance liquid chromatography (HPLC) using an Agilent Pursuit 5 C18 column (5 mm bead size, 150×21.2 mm^2) on an Agilent PrepStar 218 series preparative HPLC. Mobile phase A was water +0.1% TFA, and mobile phase B was acetonitrile +0.1% TFA. The peptide product fractions were collected, combined, and had solvent removed under reduced atmosphere. The peptide substrate was solubilized in DMSO to a final concentration of 50 mM. Purity was confirmed by liquid chromatography−mass spectrometry, and the stock was stored at −20 °C.

Assays against M[pro]. Recombinant SARS-CoV-2 M[pro] was expressed and purified as described previously in Mellot et al.[47] M[pro] activity was measured using the fluorogenic substrate, ATLQAIAS, on a Biotek Synergy HTX plate reader. All assays were performed in black flat-bottom 384-well plates, in 30 μL of 50 mM Tris-HCl pH 7.5, 150 mM NaCl, 1 mM EDTA, 0.01% Tween-20 using 50 nM M[pro] and 10 μM of FRET substrate. Initial screening was performed at 10 μM. Prior to addition of the substrate, enzyme was incubated with the compounds for 15 min. Following the substrate addition, proteolysis was measured at 320/420 nm (excitation/emission) at 25 °C. Percent inhibition was calculated relative to control reactions containing a maximum of 0.5% DMSO. Half-maximal inhibitory concentration (IC$_{50}$) was determined by nonlinear regression analysis of the velocity vs inhibitor concentration plot using GraphPad Prism 6 (GraphPad Prism, version 6.00, La Jolla, California, USA). Two independent experiments were performed in triplicate wells. At least seven inhibitor concentrations were used to build each curve. DMSO was used as negative control. The hit compounds **191**, **382**, and **415** were also tested without incubation to investigate the time-dependency behavior. Compounds **382** and **415** were evaluated in the presence of 0.1 or 1 mM DTT and otherwise identical assay conditions to the standard assay.

Reversibility Assay. M^{pro} at 100-fold its final assay concentration was incubated with the hits at 10-fold its respective IC$_{50}$ value for 30 min in a volume of 2 μL. This mixture was diluted 100-fold with an assay buffer containing 10 μM ATLQAIAS substrate to a final volume of 30 μL, resulting in a standard concentration of M^{pro} and 0.1-times the IC$_{50}$ value of hits.[130,131] Fluorescence intensities were monitored continuously during substrate hydrolysis on Synergy 2 (BioTek) plate reader for 120 min.

Assays against PL^{pro}. Recombinant SARS-CoV-2 PL^{pro} was purchased from Acro Biosystems, PAE-C5184. Proteolytic activity was measured using Z-Arg-Leu-Arg-Gly-Gly-AMC substrate (Bachem, 369 I1690) as described previously in Ashhurst et al.[156] The release of fluorescent 7-amido-4-methylcoumarin was measured at 360 nm/460 nm wavelengths for excitation/emission, on a Biotek Synergy HTX. All assays were performed in 384-well black plate at 25 °C, in a final volume of 30 μL of 50 mM HEPES pH 6.5, 150 mM NaCl, 0.1 mM DTT, 0.01% Tween-20, 50 nM enzyme, and 50 μM of substrate. Enzymatic activity was calculated by comparison to initial rates of reaction of a DMSO control. Initial screening was performed at 10 μM of each compound in triplicate wells. Compounds that inhibited by 75% or more of the PL^{pro} activity in the initial screen had their IC$_{50}$ determined. At least two independent experiments were performed, each involving at least 11 compound concentrations in triplicates. IC$_{50}$ curves were obtained by nonlinear regressions analysis of the velocity vs inhibitor concentration using GraphPad Prism 6 (GraphPad Prism, version 6.00, La Jolla, California, USA). Reported IC$_{50}$ values refer to the mean values and the standard error of the mean.

Antiviral Activity. Antiviral assays were performed according to the protocol previously described by Mellot et al.[47] Compounds **189**, **191**, **382**, and **415** were evaluated in a SARS-CoV-2 viral infection assay of monkey-derived Vero E6 cells and human-derived HeLa cells that overexpress ACE2. Remdesivir was employed as a positive control. Each compound was evaluated in ten concentrations, in 2-fold dilutions, from 20 μM to 39 nM in the case of remdesivir and from 1.0 μM to 1.9 nM for all other compounds, in triplicates.

■ ASSOCIATED CONTENT

Data Availability Statement

Prepared structures, virtual screening results, MD trajectories, MD simulation configuration and parameter files, as well as raw and processed data for protein–ligand interactions are available in the Zenodo repository (10.5281/zenodo.6598385). Crystallographic structures used are available from https://www.rcsb.org/. Third-party software employed in the manuscript were as follows. ChemBioDraw Ultra version 18.0 (https://perkinelmerinformatics.com/) is distributed under license. GraphPad PRISM version 6.0 (https://www.graphpad.com/) is distributed under license. Schrödinger Suite 2021.2 (https://www.schrodinger.com) is distributed under license. PyMOL version 2.4 (https://pymol.org/) is distributed under license. LUNA version 0.11.4 (https://github.com/keiserlab/luna) is released under the MIT open-source software license. UCSF Chimera version 15 (https://www.cgl.ucsf.edu/chimera/) is licensed for noncommercial use. Autodock Vina version 1.2 (https://vina.scripps.edu/) is an open-source free software. R version 4.1.2 (https://www.r-project.org/) is an open-source free software.

■ Supporting Information

The Supporting Information is available free of charge at https://pubs.acs.org/doi/10.1021/acs.jcim.2c00693.

General information on assembly of chemical library, structural information on all virtual screened compounds, detailed information on computational procedures, SARS-CoV-2 viral infection assay, ^{1}H and ^{13}C NMR spectra for compounds in this manuscript (PDF)

■ AUTHOR INFORMATION

Corresponding Authors

Anthony J. O'Donoghue − *Skaggs School of Pharmacy and Pharmaceutical Sciences, University of California San Diego, La Jolla, California 92093-0657, United States;* ⬤ orcid.org/0000-0001-5695-0409; Email: ajodonoghue@health.ucsd.edu

Eufrânio N. da Silva Júnior − *Institute of Exact Sciences, Department of Chemistry, Federal University of Minas Gerais, Belo Horizonte, Minas Gerais 31270-901, Brazil;* Email: eufranio@ufmg.br

Rafaela S. Ferreira − *Department of Biochemistry and Immunology, Federal University of Minas Gerais, Belo Horizonte, Minas Gerais 31270-901, Brazil;* ⬤ orcid.org/0000-0003-3324-0601; Email: rafaelasf@icb.ufmg.br

Authors

Lucianna H. Santos − *Department of Biochemistry and Immunology, Federal University of Minas Gerais, Belo Horizonte, Minas Gerais 31270-901, Brazil;* Present Address: Biomolecular Simulations Group, Institut Pasteur de Montevideo, Mataojo 2020, CP 11400 Montevideo, Uruguay

Thales Kronenberger − *Department of Oncology and Pneumonology, Internal Medicine VIII, University Hospital Tübingen, DE72076 Tübingen, Germany; School of Pharmacy, Faculty of Health Sciences, University of Eastern Finland, 70211 Kuopio, Finland; Institute of Pharmacy, Pharmaceutical/Medicinal Chemistry and Tübingen Center for Academic Drug Discovery (TüCAD2), Eberhard Karls University Tübingen, 72076 Tübingen, Germany;* ⬤ orcid.org/0000-0001-6933-7590

Renata G. Almeida − *Institute of Exact Sciences, Department of Chemistry, Federal University of Minas Gerais, Belo Horizonte, Minas Gerais 31270-901, Brazil*

Elany B. Silva − *Skaggs School of Pharmacy and Pharmaceutical Sciences, University of California San Diego, La Jolla, California 92093-0657, United States;* ⬤ orcid.org/0000-0002-1926-3500

Rafael E. O. Rocha − *Department of Biochemistry and Immunology, Federal University of Minas Gerais, Belo Horizonte, Minas Gerais 31270-901, Brazil*

Joyce C. Oliveira − *Institute of Exact Sciences, Department of Chemistry, Federal University of Minas Gerais, Belo Horizonte, Minas Gerais 31270-901, Brazil*

Luiza V. Barreto − *Department of Biochemistry and Immunology, Federal University of Minas Gerais, Belo Horizonte, Minas Gerais 31270-901, Brazil*

Danielle Skinner − *Skaggs School of Pharmacy and Pharmaceutical Sciences, University of California San Diego, La Jolla, California 92093-0657, United States*

Pavla Fajtová − *Skaggs School of Pharmacy and Pharmaceutical Sciences, University of California San Diego, La Jolla, California 92093-0657, United States; Institute of*

Organic Chemistry and Biochemistry, Academy of Sciences of the Czech Republic, 16610 Prague, Czech Republic

Miriam A. Giardini − *Skaggs School of Pharmacy and Pharmaceutical Sciences, University of California San Diego, La Jolla, California 92093-0657, United States*

Brendon Woodworth − *Department of Medicine, Division of Infectious Diseases, University of California San Diego, La Jolla, California 92093, United States*

Conner Bardine − *Department of Pharmaceutical Chemistry, University of California San Francisco, San Francisco, California 94143, United States;* ⊙ orcid.org/0000-0003-4889-2944

André L. Lourenço − *Department of Pharmaceutical Chemistry, University of California San Francisco, San Francisco, California 94143, United States*

Charles S. Craik − *Department of Pharmaceutical Chemistry, University of California San Francisco, San Francisco, California 94143, United States;* ⊙ orcid.org/0000-0001-7704-9185

Antti Poso − *Department of Oncology and Pneumonology, Internal Medicine VIII, University Hospital Tübingen, DE72076 Tübingen, Germany; School of Pharmacy, Faculty of Health Sciences, University of Eastern Finland, 70211 Kuopio, Finland;* ⊙ orcid.org/0000-0003-4196-4204

Larissa M. Podust − *Skaggs School of Pharmacy and Pharmaceutical Sciences, University of California San Diego, La Jolla, California 92093-0657, United States;* ⊙ orcid.org/0000-0002-8537-8760

James H. McKerrow − *Skaggs School of Pharmacy and Pharmaceutical Sciences, University of California San Diego, La Jolla, California 92093-0657, United States;* ⊙ orcid.org/0000-0002-5152-4627

Jair L. Siqueira-Neto − *Skaggs School of Pharmacy and Pharmaceutical Sciences, University of California San Diego, La Jolla, California 92093-0657, United States;* ⊙ orcid.org/0000-0001-9574-8174

Complete contact information is available at:
https://pubs.acs.org/10.1021/acs.jcim.2c00693

Author Contributions

L.H.S. analyzed PDB structures and interaction patterns; L.H.S., R.E.O.R., and R.S.F. performed and analyzed virtual screening results; T.K. and A.P. performed and analyzed molecular dynamics simulations; R.G.A. and E.N.S.J. designed the chemical library for virtual screening; C.B., A.L.L., and C.S.C. designed and synthesized the M^pro substrate. D.S., E.B.S., and A.J.O. performed M^pro and PL^pro assays; J.C.O., L.V.B., and T.K. performed docking studies; P.F., D.S., L.M.P., J.H.M., and A.J.O. expressed and purified M^pro; M.A.G., B.W., and J.L.S.N. performed antiviral assays. All authors were involved in experiment design and analyses; L.H.S., T.K., R.G.A., E.B.S., E.N.S.J., and R.S.F. wrote the manuscript, with revisions and contributions from all authors. E.N.S.J. and R.S.F. conceived the overall design of the study.

■ ACKNOWLEDGMENTS

■ ABBREVIATIONS

CCR2 = CC chemokine receptor 2
CCL2 = CC chemokine ligand 2
CCR5 = CC chemokine receptor 5
MD = molecular dynamics
TLC = thin layer chromatography

■ REFERENCES

(1) Gorbalenya, A. E.; Baker, S. C.; Baric, R. S.; de Groot, R. J.; Drosten, C.; Gulyaeva, A. A.; Haagmans, B. L.; Lauber, C.; Leontovich, A. M.; Neuman, B. W.; Penzar, D.; Perlman, S.; Poon, L. L. M.; Samborskiy, D. V.; Sidorov, I. A.; Sola, I.; Ziebuhr, J. The Species Severe Acute Respiratory Syndrome-Related Coronavirus: Classifying 2019-NCoV and Naming It SARS-CoV-2. *Nat. Microbiol.* **2020**, *5* (4), 536−544.

(2) Zhou, P.; Yang, X. L.; Wang, X. G.; Hu, B.; Zhang, L.; Zhang, W.; Si, H. R.; Zhu, Y.; Li, B.; Huang, C. L.; Chen, H. D.; Chen, J.; Luo, Y.; Guo, H.; Jiang, R. Di; Liu, M. Q.; Chen, Y.; Shen, X. R.; Wang, X.; Zheng, X. S.; Zhao, K.; Chen, Q. J.; Deng, F.; Liu, L. L.; Yan, B.; Zhan, F. X.; Wang, Y. Y.; Xiao, G. F.; Shi, Z. L. A Pneumonia Outbreak Associated with a New Coronavirus of Probable Bat Origin. *Nature* **2020**, *579* (7798), 270−273.

(3) Shereen, M. A.; Khan, S.; Kazmi, A.; Bashir, N.; Siddique, R. COVID-19 Infection: Origin, Transmission, and Characteristics of Human Coronaviruses. *J. Adv. Res.* **2020**, *24*, 91−98.

(4) Phan, L. T.; Nguyen, T. V.; Luong, Q. C.; Nguyen, T. V.; Nguyen, H. T.; Le, H. Q.; Nguyen, T. T.; Cao, T. M.; Pham, Q. D. Importation and Human-to-Human Transmission of a Novel Coronavirus in Vietnam. *N. Engl. J. Med.* **2020**, *382* (9), 872−874.

(5) Liu, J.; Zheng, X.; Tong, Q.; Li, W.; Wang, B.; Sutter, K.; Trilling, M.; Lu, M.; Dittmer, U.; Yang, D. Overlapping and Discrete Aspects of

the Pathology and Pathogenesis of the Emerging Human Pathogenic Coronaviruses SARS-CoV, MERS-CoV, and 2019-NCoV. *J. Med. Virol.* **2020**, *92* (5), 491−494.

(6) Zhu, N.; Zhang, D.; Wang, W.; Li, X.; Yang, B.; Song, J.; Zhao, X.; Huang, B.; Shi, W.; Lu, R.; Niu, P.; Zhan, F.; Ma, X.; Wang, D.; Xu, W.; Wu, G.; Gao, G. F.; Tan, W. A Novel Coronavirus from Patients with Pneumonia in China, 2019. *N. Engl. J. Med.* **2020**, *382* (8), 727−733.

(7) Drayman, N.; DeMarco, J. K.; Jones, K. A.; Azizi, S. A.; Froggatt, H. M.; Tan, K.; Maltseva, N. I.; Chen, S.; Nicolaescu, V.; Dvorkin, S.; Furlong, K.; Kathayat, R. S.; Firpo, M. R.; Mastrodomenico, V.; Bruce, E. A.; Schmidt, M. M.; Jedrzejczak, R.; Muñoz-Alía, M.; Schuster, B.; Nair, V.; Han, K. Y.; O'Brien, A.; Tomatsidou, A.; Meyer, B.; Vignuzzi, M.; Missiakas, D.; Botten, J. W.; Brooke, C. B.; Lee, H.; Baker, S. C.; Mounce, B. C.; Heaton, N. S.; Severson, W. E.; Palmer, K. E.; Dickinson, B. C.; Joachimiak, A.; Randall, G.; Tay, S. Masitinib Is a Broad Coronavirus 3CL Inhibitor That Blocks Replication of SARS-CoV-2. *Science (80-.)* **2021**, *373* (6557), 931−936.

(8) Ullrich, S.; Nitsche, C. The SARS-CoV-2 Main Protease as Drug Target. *Bioorg. Med. Chem. Lett.* **2020**, *30* (17), 127377.

(9) Rut, W.; Lv, Z.; Zmudzinski, M.; Patchett, S.; Nayak, D.; Snipas, S. J.; Oualid, F. El; Huang, T. T.; Bekes, M.; Drag, M.; Olsen, S. K. Activity Profiling and Crystal Structures of Inhibitor-Bound SARS-CoV-2 Papain-like Protease: A Framework for Anti−COVID-19 Drug Design. *Sci. Adv.* **2020**, *6* (42), eabd4596.

(10) Báez-Santos, Y. M.; St. John, S. E.; Mesecar, A. D. The SARS-Coronavirus Papain-like Protease: Structure, Function and Inhibition by Designed Antiviral Compounds. *Antiviral Res.* **2015**, *115*, 21−38.

(11) Wu, C.; Liu, Y.; Yang, Y.; Zhang, P.; Zhong, W.; Wang, Y.; Wang, Q.; Xu, Y.; Li, M.; Li, X.; Zheng, M.; Chen, L.; Li, H. Analysis of Therapeutic Targets for SARS-CoV-2 and Discovery of Potential Drugs by Computational Methods. *Acta Pharm. Sin. B* **2020**, *10* (5), 766−788.

(12) Kim, Y.; Liu, H.; Galasiti Kankanamalage, A. C.; Weerasekara, S.; Hua, D. H.; Groutas, W. C.; Chang, K. O.; Pedersen, N. C. Reversal of the Progression of Fatal Coronavirus Infection in Cats by a Broad-Spectrum Coronavirus Protease Inhibitor. *PLoS Pathog.* **2016**, *12* (3), No. e1005531.

(13) Zhang, L.; Lin, D.; Kusov, Y.; Nian, Y.; Ma, Q.; Wang, J.; Von Brunn, A.; Leyssen, P.; Lanko, K.; Neyts, J.; De Wilde, A.; Snijder, E. J.; Liu, H.; Hilgenfeld, R. α-Ketoamides as Broad-Spectrum Inhibitors of Coronavirus and Enterovirus Replication: Structure-Based Design, Synthesis, and Activity Assessment. *J. Med. Chem.* **2020**, *63* (9), 4562−4578.

(14) Yang, H.; Xie, W.; Xue, X.; Yang, K.; Ma, J.; Liang, W.; Zhao, Q.; Zhou, Z.; Pei, D.; Ziebuhr, J.; Hilgenfeld, R.; Kwok, Y. Y.; Wong, L.; Gao, G.; Chen, S.; Chen, Z.; Ma, D.; Bartlam, M.; Rao, Z. Design of Wide-Spectrum Inhibitors Targeting Coronavirus Main Proteases. *PLoS Biol.* **2005**, *3* (10), No. e324.

(15) Anand, K.; Palm, G. J.; Mesters, J. R.; Siddell, S. G.; Ziebuhr, J.; Hilgenfeld, R. Structure of Coronavirus Main Proteinase Reveals Combination of a Chymotrypsin Fold with an Extra α-Helical Domain. *EMBO J.* **2002**, *21* (13), 3213−3224.

(16) Yang, H.; Yang, M.; Ding, Y.; Liu, Y.; Lou, Z.; Zhou, Z.; Sun, L.; Mo, L.; Ye, S.; Pang, H.; Gao, G. F.; Anand, K.; Bartlam, M.; Hilgenfeld, R.; Rao, Z. The Crystal Structures of Severe Acute Respiratory Syndrome Virus Main Protease and Its Complex with an Inhibitor. *Proc. Natl. Acad. Sci. U. S. A.* **2003**, *100* (23), 13190−13195.

(17) Xue, X.; Yu, H.; Yang, H.; Xue, F.; Wu, Z.; Shen, W.; Li, J.; Zhou, Z.; Ding, Y.; Zhao, Q.; Zhang, X. C.; Liao, M.; Bartlam, M.; Rao, Z. Structures of Two Coronavirus Main Proteases: Implications for Substrate Binding and Antiviral Drug Design. *J. Virol.* **2008**, *82* (5), 2515−2527.

(18) Pillaiyar, T.; Manickam, M.; Namasivayam, V.; Hayashi, Y.; Jung, S. H. An Overview of Severe Acute Respiratory Syndrome-Coronavirus (SARS-CoV) 3CL Protease Inhibitors: Peptidomimetics and Small Molecule Chemotherapy. *J. Med. Chem.* **2016**, *59* (14), 6595−6628.

(19) Dai, W.; Zhang, B.; Jiang, X. M.; Su, H.; Li, J.; Zhao, Y.; Xie, X.; Jin, Z.; Peng, J.; Liu, F.; Li, C.; Li, Y.; Bai, F.; Wang, H.; Cheng, X.; Cen, X.; Hu, S.; Yang, X.; Wang, J.; Liu, X.; Xiao, G.; Jiang, H.; Rao, Z.; Zhang, L. K.; Xu, Y.; Yang, H.; Liu, H. Structure-Based Design of

Antiviral Drug Candidates Targeting the SARS-CoV-2 Main Protease. *Science (80-.)* **2020**, *368* (6497), 1331−1335.

(20) Sacco, M. D.; Ma, C.; Lagarias, P.; Gao, A.; Townsend, J. A.; Meng, X.; Dube, P.; Zhang, X.; Hu, Y.; Kitamura, N.; Hurst, B.; Tarbet, B.; Marty, M. T.; Kolocouris, A.; Xiang, Y.; Chen, Y.; Wang, J. Structure and Inhibition of the SARS-CoV-2 Main Protease Reveal Strategy for Developing Dual Inhibitors against Mpro and Cathepsin L. *Sci. Adv.* **2020**, *6* (50), eabe0751.

(21) Hung, H. C.; Ke, Y. Y.; Huang, S. Y.; Huang, P. N.; Kung, Y. A.; Chang, T. Y.; Yen, K. J.; Peng, T. T.; Chang, S. E.; Huang, C. T.; Tsai, Y. R.; Wu, S. H.; Lee, S. J.; Lin, J. H.; Liu, B. S.; Sung, W. C.; Shih, S. R.; Chen, C. T.; Hsu, J. T. A. Discovery of M Protease Inhibitors Encoded by SARS-CoV-2. *Antimicrob. Agents Chemother.*. **2020**, *64* (9). DOI: 10.1128/AAC.00872-20.

(22) Zhang, L.; Lin, D.; Sun, X.; Curth, U.; Drosten, C.; Sauerhering, L.; Becker, S.; Rox, K.; Hilgenfeld, R. Crystal Structure of SARS-CoV-2 Main Protease Provides a Basis for Design of Improved a-Ketoamide Inhibitors. *Science (80-.)* **2020**, *368* (6489), 409−412.

(23) Ma, C.; Sacco, M. D.; Hurst, B.; Townsend, J. A.; Hu, Y.; Szeto, T.; Zhang, X.; Tarbet, B.; Marty, M. T.; Chen, Y.; Wang, J. Boceprevir, GC-376, and Calpain Inhibitors II, XII Inhibit SARS-CoV-2 Viral Replication by Targeting the Viral Main Protease. *Cell Res.* **2020**, *30* (8), 678−692.

(24) Jin, Z.; Du, X.; Xu, Y.; Deng, Y.; Liu, M.; Zhao, Y.; Zhang, B.; Li, X.; Zhang, L.; Peng, C.; Duan, Y.; Yu, J.; Wang, L.; Yang, K.; Liu, F.; Jiang, R.; Yang, X.; You, T.; Liu, X.; Yang, X.; Bai, F.; Liu, H.; Liu, X.; Guddat, L. W.; Xu, W.; Xiao, G.; Qin, C.; Shi, Z.; Jiang, H.; Rao, Z.; Yang, H. Structure of Mpro from SARS-CoV-2 and Discovery of Its Inhibitors. *Nature* **2020**, *582* (7811), 289−293.

(25) Zhang, C. H.; Stone, E. A.; Deshmukh, M.; Ippolito, J. A.; Ghahremanpour, M. M.; Tirado-Rives, J.; Spasov, K. A.; Zhang, S.; Takeo, Y.; Kudalkar, S. N.; Liang, Z.; Isaacs, F.; Lindenbach, B.; Miller, S. J.; Anderson, K. S.; Jorgensen, W. L. Potent Noncovalent Inhibitors of the Main Protease of SARS-CoV-2 from Molecular Sculpting of the Drug Perampanel Guided by Free Energy Perturbation Calculations. *ACS Cent. Sci.* **2021**, *7* (3), 467−475.

(26) Su, H.; Yao, S.; Zhao, W.; Zhang, Y.; Liu, J.; Shao, Q.; Wang, Q.; Li, M.; Xie, H.; Shang, W.; Ke, C.; Feng, L.; Jiang, X.; Shen, J.; Xiao, G.; Jiang, H.; Zhang, L.; Ye, Y.; Xu, Y. Identification of Pyrogallol as a Warhead in Design of Covalent Inhibitors for the SARS-CoV-2 3CL Protease. *Nat. Commun.* **2021**, *12* (1), 3623.

(27) Oerlemans, R.; Ruiz-Moreno, A. J.; Cong, Y.; Dinesh Kumar, N.; Velasco-Velazquez, M. A.; Neochoritis, C. G.; Smith, J.; Reggiori, F.; Groves, M. R.; Dömling, A. Repurposing the HCV NS3−4A Protease Drug Boceprevir as COVID-19 Therapeutics. *RSC Med. Chem.* **2021**, *12* (3), 370−379.

(28) Kneller, D. W.; Phillips, G.; Weiss, K. L.; Zhang, Q.; Coates, L.; Kovalevsky, A. Direct Observation of Protonation State Modulation in SARS-CoV-2 Main Protease upon Inhibitor Binding with Neutron Crystallography. *J. Med. Chem.* **2021**, *64* (8), 4991−5000.

(29) Günther, S.; Reinke, P. Y. A.; Fernández-García, Y.; Lieske, J.; Lane, T. J.; Ginn, H. M.; Koua, F. H. M.; Ehrt, C.; Ewert, W.; Oberthuer, D. X-Ray Screening Identifies Active Site and Allosteric Inhibitors of SARS-CoV-2 Main Protease. *Science (80-.)* **2021**, *372*, 642.

(30) Owen, D. R.; Allerton, C. M. N.; Anderson, A. S.; Aschenbrenner, L.; Avery, M.; Berritt, S.; Boras, B.; Cardin, R. D.; Carlo, A.; Coffman, K. J.; Dantonio, A.; Di, L.; Eng, H.; Ferre, R. A.; Gajiwala, K. S.; Gibson, S. A.; Greasley, S. E.; Hurst, B. L.; Kadar, E. P.; Kalgutkar, A. S.; Lee, J. C.; Lee, J.; Liu, W.; Mason, S. W.; Noell, S.; Novak, J. J.; Obach, R. S.; Ogilvie, K.; Patel, N. C.; Pettersson, M.; Rai, D. K.; Reese, M. R.; Sammons, M. F.; Sathish, J. G.; Singh, R. S. P.; Steppan, C. M.; Stewart, A. E.; Tuttle, J. B.; Updyke, L.; Verhoest, P. R.; Wei, L.; Yang, Q.; Zhu, Y. An Oral SARS-CoV-2 Mpro Inhibitor Clinical Candidate for the Treatment of COVID-19. *Science (80-.)* **2021**, *374* (6575), 1586−1593.

(31) Báez-Santos, Y. M.; Barraza, S. J.; Wilson, M. W.; Agius, M. P.; Mielech, A. M.; Davis, N. M.; Baker, S. C.; Larsen, S. D.; Mesecar, A. D. X-Ray Structural and Biological Evaluation of a Series of Potent and Highly Selective Inhibitors of Human Coronavirus Papain-like Proteases. *J. Med. Chem.* **2014**, *57* (6), 2393−2412.

P

(32) Ratia, K.; Pegan, S.; Takayama, J.; Sleeman, K.; Coughlin, M.; Baliji, S.; Chaudhuri, R.; Fu, W.; Prabhakar, B. S.; Johnson, M. E.; Baker, S. C.; Ghosh, A. K.; Mesecar, A. D. A Noncovalent Class of Papain-like Protease/Deubiquitinase Inhibitors Blocks SARS Virus Replication. *Proc. Natl. Acad. Sci. U. S. A.* **2008**, *105* (42), 16119−16124.

(33) Lin, M. H.; Moses, D. C.; Hsieh, C. H.; Cheng, S. C.; Chen, Y. H.; Sun, C. Y.; Chou, C. Y. Disulfiram Can Inhibit MERS and SARS Coronavirus Papain-like Proteases via Different Modes. *Antiviral Res.* **2018**, *150*, 155−163.

(34) Lei, J.; Kusov, Y.; Hilgenfeld, R. Nsp3 of Coronaviruses: Structures and Functions of a Large Multi-Domain Protein. *Antiviral Res.* **2018**, *149*, 58−74.

(35) Armstrong, L. A.; Lange, S. M.; Cesare, V. D.; Matthews, S. P.; Nirujogi, R. S.; Cole, I.; Hope, A.; Cunningham, F.; Toth, R.; Mukherjee, R.; Bojkova, D.; Gruber, F.; Gray, D.; Wyatt, P. G.; Cinatl, J.; Dikic, I.; Davies, P.; Kulathu, Y. Biochemical Characterization of Protease Activity of Nsp3 from SARS-CoV-2 and Its Inhibition by Nanobodies. *PLoS One* **2021**, *16*, No. e0253364.

(36) Osipiuk, J.; Azizi, S. A.; Dvorkin, S.; Endres, M.; Jedrzejczak, R.; Jones, K. A.; Kang, S.; Kathayat, R. S.; Kim, Y.; Lisnyak, V. G.; Maki, S. L.; Nicolaescu, V.; Taylor, C. A.; Tesar, C.; Zhang, Y. A.; Zhou, Z.; Randall, G.; Michalska, K.; Snyder, S. A.; Dickinson, B. C.; Joachimiak, A. Structure of Papain-like Protease from SARS-CoV-2 and Its Complexes with Non-Covalent Inhibitors. *Nat. Commun.* **2021**, *12* (1), 1−9.

(37) Fu, Z.; Huang, B.; Tang, J.; Liu, S.; Liu, M.; Ye, Y.; Liu, Z.; Xiong, Y.; Zhu, W.; Cao, D.; Li, J.; Niu, X.; Zhou, H.; Zhao, Y. J.; Zhang, G.; Huang, H. The Complex Structure of GRL0617 and SARS-CoV-2 PLpro Reveals a Hot Spot for Antiviral Drug Discovery. *Nat. Commun.* **2021**, *12* (1), 1−12.

(38) Shan, H.; Liu, J.; Shen, J.; Dai, J.; Xu, G.; Lu, K.; Han, C.; Wang, Y.; Xu, X.; Tong, Y.; Xiang, H.; Ai, Z.; Zhuang, G.; Hu, J.; Zhang, Z.; Li, Y.; Pan, L.; Tan, L. Development of Potent and Selective Inhibitors Targeting the Papain-like Protease of SARS-CoV-2. *Cell Chem. Biol.* **2021**, *28* (6), 855−865.e9.

(39) Shen, Z.; Ratia, K.; Cooper, L.; Kong, D.; Lee, H.; Kwon, Y.; Li, Y.; Alqarni, S.; Huang, F.; Dubrovskyi, O.; Rong, L.; Thatcher, G. R. J.; Xiong, R. Design of SARS-CoV-2 PLpro Inhibitors for COVID-19 Antiviral Therapy Leveraging Binding Cooperativity. *J. Med. Chem.* **2022**, *65* (4), 2940−2955.

(40) Gao, X.; Qin, B.; Chen, P.; Zhu, K.; Hou, P.; Wojdyla, J. A.; Wang, M.; Cui, S. Crystal Structure of SARS-CoV-2 Papain-like Protease. *Acta Pharm. Sin. B* **2021**, *11* (1), 237−245.

(41) Klemm, T.; Ebert, G.; Calleja, D. J.; Allison, C. C.; Richardson, L. W.; Bernardini, J. P.; Lu, B. G. C.; Kuchel, N. W.; Grohmann, C.; Shibata, Y.; Gan, Z. Y.; Cooney, J. P.; Doerflinger, M.; Au, A. E.; Blackmore, T. R.; Geurink, P. P.; Ovaa, H.; Newman, J.; Riboldi-Tunnicliffe, A.; Czabotar, P. E.; Mitchell, J. P.; Feltham, R.; Lechtenberg, B. C.; Lowes, K. N.; Dewson, G.; Pellegrini, M.; Lessene, G.; Komander, D. Mechanism and Inhibition of SARS-CoV-2 PLpro. *bioRxiv* **2020**, *39* (18), 1−17.

(42) Pushpakom, S.; Iorio, F.; Eyers, P. A.; Escott, K. J.; Hopper, S.; Wells, A.; Doig, A.; Guilliams, T.; Latimer, J.; McNamee, C.; et al. Drug Repurposing: Progress, Challenges and Recommendations. *Nat. Rev. Drug Discovery* **2019**, *18* (1), 41−58.

(43) Li, G.; De Clercq, E. Therapeutic Options for the 2019 Novel Coronavirus (2019-NCoV). *Nat. Rev. Drug Discovery* **2020**, *19* (3), 149−150.

(44) Da Cruz, E. H. G.; Hussene, C. M. B.; Dias, G. G.; Diogo, E. B. T.; De Melo, I. M. M.; Rodrigues, B. L.; Da Silva, M. G.; Valença, W. O.; Camara, C. A.; De Oliveira, R. N.; De Paiva, Y. G.; Goulart, M. O. F.; Cavalcanti, B. C.; Pessoa, C.; Da Silva Júnior, E. N. 1,2,3-Triazole-, Arylamino- and Thio-Substituted 1,4-Naphthoquinones: Potent Antitumor Activity, Electrochemical Aspects, and Bioisosteric Replacement of C-Ring-Modified Lapachones. *Bioorg. Med. Chem.* **2014**, *22* (5), 1608−1619.

(45) de Carvalho, R. L.; Jardim, G. A. M.; Santos, A. C. C.; Araujo, M. H.; Oliveira, W. X. C.; Bombaça, A. C. S.; Menna-Barreto, R. F. S.; Gopi, E.; Gravel, E.; Doris, E.; da Silva Júnior, E. N. Combination of

(46) Aryl Diselenides/Hydrogen Peroxide and Carbon-Nanotube/Rhodium Nanohybrids for Naphthol Oxidation: An Efficient Route towards Trypanocidal Quinones. *Chemistry* **2018**, *24* (57), 15227−15235.

(46) Jardim, G. A. M.; Silva, T. L.; Goulart, M. O. F.; de Simone, C. A.; Barbosa, J. M. C.; Salomão, K.; de Castro, S. L.; Bower, J. F.; da Silva Júnior, E. N. Rhodium-Catalyzed C-H Bond Activation for the Synthesis of Quinonoid Compounds: Significant Anti-Trypanosoma Cruzi Activities and Electrochemical Studies of Functionalized Quinones. *Eur. J. Med. Chem.* **2017**, *136*, 406−419.

(47) Mellott, D. M.; Tseng, C. Te; Drelich, A.; Fajtová, P.; Chenna, B. C.; Kostomiris, D. H.; Hsu, J.; Zhu, J.; Taylor, Z. W.; Kocurek, K. I.; Tat, V.; Katzfuss, A.; Li, L.; Giardini, M. A.; Skinner, D.; Hirata, K.; Yoon, M. C.; Beck, S.; Carlin, A. F.; Clark, A. E.; Beretta, L.; Maneval, D.; Hook, V.; Frueh, F.; Hurst, B. L.; Wang, H.; Raushel, F. M.; O'Donoghue, A. J.; De Siqueira-Neto, J. L.; Meek, T. D.; McKerrow, J. H. A Clinical-Stage Cysteine Protease Inhibitor Blocks SARS-CoV-2 Infection of Human and Monkey Cells. *ACS Chem. Biol.* **2021**, *16* (4), 642−650.

(48) Lu, R.; Zhao, X.; Li, J.; Niu, P.; Yang, B.; Wu, H.; Wang, W.; Song, H.; Huang, B.; Zhu, N.; Bi, Y.; Ma, X.; Zhan, F.; Wang, L.; Hu, T.; Zhou, H.; Hu, Z.; Zhou, W.; Zhao, L.; Chen, J.; Meng, Y.; Wang, J.; Lin, Y.; Yuan, J.; Xie, Z.; Ma, J.; Liu, W. J.; Wang, D.; Xu, W.; Holmes, E. C.; Gao, G. F.; Wu, G.; Chen, W.; Shi, W.; Tan, W. Genomic Characterisation and Epidemiology of 2019 Novel Coronavirus: Implications for Virus Origins and Receptor Binding. *Lancet* **2020**, *395* (10224), 565−574.

(49) *Gilead's Investigational Antiviral Remdesivir Receives U.S. Food and Drug Administration Emergency Use Authorization for the Treatment of COVID-19*; Gilead Sciences Inc., 2020. https://www.gilead.com/news-and-press/press-room/press-releases/2020/5/gileads-investigational-antiviral-remdesivir-receives-us-food-and-drug-administration-emergency-use-authorization-for-the-treatment-of-covid19 (accessed 04-21-2021).

(50) *Fact Sheet for Health Care Providers Emergency Use Authorization of Bamlanivimab and Etesevimab*; U.S. Food and Drug Administration, 2021. https://www.fda.gov/media/145802/download#:~:text=Bamlanivimab%20and%20etesevimab%20may%20only,(EMS)%2C%20as%20necessary. (accessed 04-21-2021).

(51) Pardo, J.; Shukla, A. M.; Chamarthi, G.; Gupte, A. The Journey of Remdesivir: From Ebola to COVID-19. *Drugs Context* **2020**, *9*, 1.

(52) Beigel, J. H.; Tomashek, K. M.; Dodd, L. E.; Mehta, A. K.; Zingman, B. S.; Kalil, A. C.; Hohmann, E.; Chu, H. Y.; Luetkemeyer, A.; Kline, S.; Lopez de Castilla, D.; Finberg, R. W.; Dierberg, K.; Tapson, V.; Hsieh, L.; Patterson, T. F.; Paredes, R.; Sweeney, D. A.; Short, W. R.; Touloumi, G.; Lye, D. C.; Ohmagari, N.; Oh, M.; Ruiz-Palacios, G. M.; Benfield, T.; Fätkenheuer, G.; Kortepeter, M. G.; Atmar, R. L.; Creech, C. B.; Lundgren, J.; Babiker, A. G.; Pett, S.; Neaton, J. D.; Burgess, T. H.; Bonnett, T.; Green, M.; Makowski, M.; Osinusi, A.; Nayak, S.; Lane, H. C. Remdesivir for the Treatment of Covid-19 — Final Report. *N. Engl. J. Med.* **2020**, *383* (19), 1813−1826.

(53) Jayk Bernal, A.; Gomes da Silva, M. M.; Musungaie, D. B.; Kovalchuk, E.; Gonzalez, A.; Delos Reyes, V.; Martín-Quirós, A.; Caraco, Y.; Williams-Diaz, A.; Brown, M. L.; Du, J.; Pedley, A.; Assaid, C.; Strizki, J.; Grobler, J. A.; Shamsuddin, H. H.; Tipping, R.; Wan, H.; Paschke, A.; Butterton, J. R.; Johnson, M. G.; De Anda, C. Molnupiravir for Oral Treatment of Covid-19 in Nonhospitalized Patients. *N. Engl. J. Med.* **2022**, *386* (6), 509−520.

(54) Hossan, M. S.; Fatima, A.; Rahmatullah, M.; Khoo, T. J.; Nissapatorn, V.; Galochkina, A. V.; Slita, A. V.; Shtro, A. A.; Nikolaeva, Y.; Zarubaev, V. V.; Wiart, C. Antiviral Activity of Embelia Ribes Burm. f. against Influenza Virus in Vitro. *Arch. Virol.* **2018**, *163* (8), 2121−2131.

(55) Parvez, M. K.; Tabish Rehman, M.; Alam, P.; Al-Dosari, M. S.; Alqasoumi, S. I.; Alajmi, M. F. Plant-Derived Antiviral Drugs as Novel Hepatitis B Virus Inhibitors: Cell Culture and Molecular Docking Study. *Saudi Pharm. J.* **2019**, *27* (3), 389−400.

(56) Caruso, F.; Rossi, M.; Pedersen, J. Z.; Incerpi, S. Computational Studies Reveal Mechanism by Which Quinone Derivatives Can Inhibit SARS-CoV-2. Study of Embelin and Two Therapeutic Compounds of

Q

Interest, Methyl Prednisolone and Dexamethasone. *J. Infect. Public Health* **2020**, *13* (12), 1868−1877.

(57) Ryu, Y. B.; Park, S. J.; Kim, Y. M.; Lee, J. Y.; Seo, W. D.; Chang, J. S.; Park, K. H.; Rho, M. C.; Lee, W. S. SARS-CoV 3CLpro Inhibitory Effects of Quinone-Methide Triterpenes from Tripterygium Regelii. *Bioorg. Med. Chem. Lett.* **2010**, *20* (6), 1873−1876.

(58) da Silva Júnior, E. N.; de Souza, M. C. B. V.; Pinto, A. V.; Pinto, M. do C. F. R.; Goulart, M. O. F.; Barros, F. W. A.; Pessoa, C.; Costa-Lotufo, L. V.; Montenegro, R. C.; de Moraes, M. O.; Ferreira, V. F. Synthesis and Potent Antitumor Activity of New Arylamino Derivatives of Nor-β-Lapachone and nor-α-Lapachone. *Bioorg. Med. Chem.* **2007**, *15* (22), 7035−7041.

(59) da Silva Júnior, E. N.; de Souza, M. C. B. V.; Fernandes, M. C.; Menna-Barreto, R. F. S.; Pinto, M. do C. F. R.; de Assis Lopes, F.; de Simone, C. A.; Andrade, C. K. Z.; Pinto, A. V.; Ferreira, V. F.; de Castro, S. L. Synthesis and Anti-Trypanosoma Cruzi Activity of Derivatives from nor-Lapachones and Lapachones. *Bioorg. Med. Chem.* **2008**, *16* (9), 5030−5038.

(60) da Silva Júnior, E. N.; Guimarães, T. T.; Menna-Barreto, R. F. S.; Pinto, M. do C. F. R.; de Simone, C. A.; Pessoa, C.; Cavalcanti, B. C.; Sabino, J. R.; Andrade, C. K. Z.; Goulart, M. O. F.; de Castro, S. L.; Pinto, A. V. The Evaluation of Quinonoid Compounds against Trypanosoma Cruzi: Synthesis of Imidazolic Anthraquinones, nor-β-Lapachone Derivatives and β-Lapachone-Based 1,2,3-Triazoles. *Bioorg. Med. Chem.* **2010**, *18* (9), 3224−3230.

(61) da Silva Junior, E. N.; de Deus, C. F.; Cavalcanti, B. C.; Pessoa, C.; Costa-Lotufo, L. V.; Montenegro, R. C.; de Moraes, M. O.; Pinto, M. d. C. F. R.; de Simone, C. A.; Ferreira, V. F.; Goulart, M. O. F.; Andrade, C. K. Z.; Pinto, A. V. 3-Arylamino and 3-Alkoxy-nor-β-Lapachone Derivatives: Synthesis and Cytotoxicity against Cancer Cell Lines. *J. Med. Chem.* **2010**, *53* (1), 504−508.

(62) De Souza, A. A.; De Moura, M. A. B. F.; De Abreu, F. C.; Goulart, M. O. F.; Da Silva, E. N.; Pinto, A. V.; Ferreira, V. F.; Moscoso, R.; Núñez-Vergara, L. J.; Squella, J. A. Electrochemical Study, on Mercury, of a Meta-Nitroarylamine Derivative of nor-β-Lapachone, an Antitumor and Trypanocidal Compound. *Quim. Nova* **2010**, *33* (10), 2075−2079.

(63) Da Cruz, E. H. G.; Silvers, M. A.; Jardim, G. A. M.; Resende, J. M.; Cavalcanti, B. C.; Bomfim, I. S.; Pessoa, C.; De Simone, C. A.; Botteselle, G. V.; Braga, A. L.; Nair, D. K.; Namboothiri, I. N. N.; Boothman, D. A.; Da Silva Júnior, E. N. Synthesis and Antitumor Activity of Selenium-Containing Quinone-Based Triazoles Possessing Two Redox Centres, and Their Mechanistic Insights. *Eur. J. Med. Chem.* **2016**, *122*, 1−16.

(64) Vieira, A. A.; Brandão, I. R.; Valença, W. O.; De Simone, C. A.; Cavalcanti, B. C.; Pessoa, C.; Carneiro, T. R.; Braga, A. L.; Da Silva, E. N. Hybrid Compounds with Two Redox Centres: Modular Synthesis of Chalcogen-Containing Lapachones and Studies on Their Antitumor Activity. *Eur. J. Med. Chem.* **2015**, *101*, 254−265.

(65) Kharma, A.; Jacob, C.; Bozzi, Í. A. O.; Jardim, G. A. M.; Braga, A. L.; Salomão, K.; Gatto, C. C.; Silva, M. F. S.; Pessoa, C.; Stangier, M.; Ackermann, L.; da Silva Júnior, E. N. Electrochemical Selenation/Cyclization of Quinones: A Rapid, Green and Efficient Access to Functionalized Trypanocidal and Antitumor Compounds. *Eur. J. Org. Chem.* **2020**, *2020* (29), 4474−4486.

(66) Almeida, R. G.; Valença, W. O.; Rosa, L. G.; De Simone, C. A.; De Castro, S. L.; Barbosa, J. M. C.; Pinheiro, D. P.; Paier, C. R. K.; De Carvalho, G. G. C.; Pessoa, C.; Goulart, M. O. F.; Kharma, A.; Da Silva Júnior, E. N. Synthesis of Quinone Imine and Sulphur-Containing Compounds with Antitumor and Trypanocidal Activities: Redox and Biological Implications. *RSC Med. Chem.* **2020**, *11* (10), 1145−1160.

(67) Jardim, G. A. M.; Guimarães, T. T.; Pinto, M. D. C. F. R.; Cavalcanti, B. C.; De Farias, K. M.; Pessoa, C.; Gatto, C. C.; Nair, D. K.; Namboothiri, I. N. N.; Da Silva Júnior, E. N. Naphthoquinone-Based Chalcone Hybrids and Derivatives: Synthesis and Potent Activity against Cancer Cell Lines. *Medchemcomm* **2015**, *6* (1), 120−150.

(68) Cavalcanti, B. C.; Cabral, I. O.; Rodrigues, F. A. R.; Barros, F. W. A.; Rocha, D. D.; Magalhães, H. I. F.; Moura, D. J.; Saffi, J.; Henriques, J. A. P.; Carvalho, T. S. C.; Moraes, M. O.; Pessoa, C.; De Melo, I. M. M.;

Da Silva, E. N. Potent Antileukemic Action of Naphthoquinoidal Compounds: Evidence for an Intrinsic Death Mechanism Based on Oxidative Stress and Inhibition of DNA Repair. *J. Braz. Chem. Soc.* **2013**, *24* (1), 145−163.

(69) De Castro, S. L.; Emery, F. S.; Da Silva Júnior, E. N. Synthesis of Quinoidal Molecules: Strategies towards Bioactive Compounds with an Emphasis on Lapachones. *Eur. J. Med. Chem.* **2013**, *69*, 678−700.

(70) Jardim, G. A. M.; Reis, W. J.; Ribeiro, M. F.; Ottoni, F. M.; Alves, R. J.; Silva, T. L.; Goulart, M. O. F.; Braga, A. L.; Menna-Barreto, R. F. S.; Salomão, K.; De Castro, S. L.; Da Silva Júnior, E. N. On the Investigation of Hybrid Quinones: Synthesis, Electrochemical Studies and Evaluation of Trypanocidal Activity. *RSC Adv.* **2015**, *5* (95), 78047−78060.

(71) Dias, G. G.; Rogge, T.; Kuniyil, R.; Jacob, C.; Menna-Barreto, R. F. S.; Da Silva Júnior, E. N.; Ackermann, L. Ruthenium-Catalyzed C-H Oxygenation of Quinones by Weak O-Coordination for Potent Trypanocidal Agents. *Chem. Commun.* **2018**, *54* (91), 12840−12843.

(72) Baiju, T. V.; Almeida, R. G.; Sivanandan, S. T.; de Simone, C. A.; Brito, L. M.; Cavalcanti, B. C.; Pessoa, C.; Namboothiri, I. N. N.; da Silva Júnior, E. N. Quinonoid Compounds via Reactions of Lawsone and 2-Aminonaphthoquinone with α-Bromonitroalkenes and Nitro-allylic Acetates: Structural Diversity by C-Ring Modification and Cytotoxic Evaluation against Cancer Cells. *Eur. J. Med. Chem.* **2018**, *151*, 686−704.

(73) Suginome, H.; Konishi, A.; Sakurai, H.; Minakawa, H.; Takeda, T.; Senboku, H.; Tokuda, M.; Kobayashi, K. Photoinduced Molecular Transformations. Part 156. New Photoadditions of 2-Hydroxy-1,4-Naphthoquinones with Naphthols and Their Derivatiyes. *Tetrahedron* **1995**, *51* (5), 1377−1386.

(74) Wood, J. M.; Satam, N. S.; Almeida, R. G.; Cristani, V. S.; de Lima, D. P.; Dantas-Pereira, L.; Salomão, K.; Menna-Barreto, R. F. S.; Namboothiri, I. N. N.; Bower, J. F.; da Silva Júnior, E. N. Strategies towards Potent Trypanocidal Drugs: Application of Rh-Catalyzed [2 + 2 + 2] Cycloadditions, Sulfonyl Phthalide Annulation and Nitroalkene Reactions for the Synthesis of Substituted Quinones and Their Evaluation against Trypanosoma Cruzi. *Bioorg. Med. Chem.* **2020**, *28* (15), No. 115565.

(75) da Silva Júnior, E. N.; de Carvalho, R. L.; Almeida, R. G.; Rosa, L. G.; Fantuzzi, F.; Rogge, T.; Costa, P. M. S.; Pessoa, C.; Jacob, C.; Ackermann, L. Ruthenium(II)-Catalyzed Double Annulation of Quinones: Step-Economical Access to Valuable Bioactive Compounds. *Chem. - A Eur. J.* **2020**, *26* (48), 10981−10986.

(76) Tandon, V. K.; Yadav, D. B.; Singh, R. V.; Vaish, M.; Chaturvedi, A. K.; Shukla, P. K. Synthesis and Biological Evaluation of Novel 1,4-Naphthoquinone Derivatives as Antibacterial and Antiviral Agents. *Bioorg. Med. Chem. Lett.* **2005**, *15* (14), 3463−3466.

(77) Krishnamoorthy, G.; Webb, S. P.; Nguyen, T.; Chowdhury, P. K.; Halder, M.; Wills, N. J.; Carpenter, S.; Kraus, G. A.; Gordon, M. S.; Petrich, J. W. Synthesis of Hydroxy and Methoxy Perylene Quinones, Their Spectroscopic and Computational Characterization, and Their Antiviral Activity¶. *Photochem. Photobiol.* **2005**, *81* (4), 924.

(78) Silva, L. R.; Guimarães, A. S.; do Nascimento, J.; do Santos Nascimento, I. J.; da Silva, E. B.; McKerrow, J. H.; Cardoso, S. H.; da Silva-Júnior, E. F. Computer-Aided Design of 1,4-Naphthoquinone-Based Inhibitors Targeting Cruzain and Rhodesain Cysteine Proteases. *Bioorg. Med. Chem.* **2021**, *41*, No. 116213.

(79) da Silva, E. N.; Menna-Barreto, R. F. S.; Pinto, M. do C. F. R.; Silva, R. S. F.; Teixeira, D. V.; de Souza, M. C. B. V.; De Simone, C. A.; De Castro, S. L.; Ferreira, V. F.; Pinto, A. V. Naphthoquinoidal [1,2,3]-Triazole, a New Structural Moiety Active against Trypanosoma Cruzi. *Eur. J. Med. Chem.* **2008**, *43* (8), 1774−1780.

(80) da Silva Júnior, E. N.; de Moura, M. A. B. F.; Pinto, A. V.; Pinto, M. do C. F. R.; de Souza, M. C. B. V.; Araújo, A. J.; Pessoa, C.; Costa-Lotufo, L. V.; Montenegro, R. C.; de Moraes, M. O.; Ferreira, V. F.; Goulart, M. O. F. Cytotoxic, Trypanocidal Activities and Physicochemical Parameters of nor-β-Lapachone-Based 1,2,3-Triazoles. *J. Braz. Chem. Soc.* **2009**, *20* (4), 635−643.

(81) Da Silva, E. N.; De Melo, I. M. M.; Diogo, E. B. T.; Costa, V. A.; De Souza Filho, J. D.; Valença, W. O.; Camara, C. A.; De Oliveira, R. N.;

De Araujo, A. S.; Emery, F. S.; Dos Santos, M. R.; De Simone, C. A.; Menna-Barreto, R. F. S.; De Castro, S. L. On the Search for Potential Anti-Trypanosoma Cruzi Drugs: Synthesis and Biological Evaluation of 2-Hydroxy-3-Methylamino and 1,2,3-Triazolic Naphthoquinoidal Compounds Obtained by Click Chemistry Reactions. *Eur. J. Med. Chem.* **2012**, *52*, 304−312.

(82) Cardoso, M. F. C.; Rodrigues, P. C.; Oliveira, M. E. I. M.; Gama, I. L.; Da Silva, I. M. C. B.; Santos, I. O.; Rocha, D. R.; Pinho, R. T.; Ferreira, V. F.; De Souza, M. C. B. V.; Da Silva, F. D. C.; Silva-Jr, F. P. Synthesis and Evaluation of the Cytotoxic Activity of 1,2-Furanonaphthoquinones Tethered to 1,2,3−1H-Triazoles in Myeloid and Lymphoid Leukemia Cell Lines. *Eur. J. Med. Chem.* **2014**, *84*, 708−717.

(83) Jardim, G. A. M.; Cruz, E. H. G.; Valença, W. O.; Resende, J. M.; Rodrigues, B. L.; Ramos, D. F.; Oliveira, R. N.; Silva, P. E. A.; Da Silva Júnior, E. N. On the Search for Potential Antimycobacterial Drugs: Synthesis of Naphthoquinoidal, Phenazinic and 1,2,3-Triazolic Compounds and Evaluation against Mycobacterium Tuberculosis. *J. Braz. Chem. Soc.* **2015**, *26* (5), 1013−1027.

(84) dos Santos, F. S.; Dias, G. G.; de Freitas, R. P.; Santos, L. S.; de Lima, G. F.; Duarte, H. A.; de Simone, C. A.; Rezende, L. M. S. L.; Vianna, M. J. X.; Correa, J. R.; Neto, B. A. D.; da Silva Júnior, E. N. Redox Center Modification of Lapachones towards the Synthesis of Nitrogen Heterocycles as Selective Fluorescent Mitochondrial Imaging Probes. *Eur. J. Org. Chem.* **2017**, *2017* (26), 3763−3773.

(85) Bahia, S. B. B.; Reis, W. J.; Jardim, G. A. M.; Souto, F. T.; De Simone, C. A.; Gatto, C. C.; Menna-Barreto, R. F. S.; De Castro, S. L.; Cavalcanti, B. C.; Pessoa, C.; Araujo, M. H.; Da Silva Júnior, E. N. Molecular Hybridization as a Powerful Tool towards Multitarget Quinoidal Systems: Synthesis, Trypanocidal and Antitumor Activities of Naphthoquinone-Based 5-Iodo-1,4-Disubstituted-, 1,4- and 1,5-Disubstituted-1,2,3-Triazoles. *Medchemcomm* **2016**, *7* (8), 1555−1563.

(86) Jardim, G. A. M.; Da Cruz, E. H. G.; Valença, W. O.; Lima, D. J. B.; Cavalcanti, B. C.; Pessoa, C.; Rafique, J.; Braga, A. L.; Jacob, C.; Da Silva, E. N.; et al. Synthesis of Selenium-Quinone Hybrid Compounds with Potential Antitumor Activity via Rh-Catalyzed C-H Bond Activation and Click Reactions. *Molecules* **2018**, *23* (1), 83.

(87) Gontijo, T. B.; De Freitas, R. P.; De Lima, G. F.; De Rezende, L. C. D.; Pedrosa, L. F.; Silva, T. L.; Goulart, M. O. F.; Cavalcanti, B. C.; Pessoa, C.; Bruno, M. P.; Corrêa, J. R.; Emery, F. S.; Da Silva Júnior, E. N. Novel Fluorescent Lapachone-Based BODIPY: Synthesis, Computational and Electrochemical Aspects, and Subcellular Localisation of a Potent Antitumour Hybrid Quinone. *Chem. Commun.* **2016**, *52* (90), 13281−13284.

(88) Gontijo, T. B.; de Freitas, R. P.; Emery, F. S.; Pedrosa, L. F.; Vieira Neto, J. B.; Cavalcanti, B. C.; Pessoa, C.; King, A.; de Moliner, F.; Vendrell, M.; da Silva Júnior, E. N. On the Synthesis of Quinone-Based BODIPY Hybrids: New Insights on Antitumor Activity and Mechanism of Action in Cancer Cells. *Bioorg. Med. Chem. Lett.* **2017**, *27* (18), 4446−4456.

(89) Valença, W. O.; Baiju, T. V.; Brito, F. G.; Araujo, M. H.; Pessoa, C.; Cavalcanti, B. C.; de simone, C. A.; Jacob, C.; Namboothiri, I. N. N.; da Silva Júnior, E. N. Synthesis of Quinone-Based N-Sulfonyl-1,2,3-Triazoles: Chemical Reactivity of Rh(II) Azavinyl Carbenes and Antitumor Activity. *ChemistrySelect* **2017**, *2* (16), 4301−4308.

(90) Diogo, E. B. T.; Dias, G. G.; Rodrigues, B. L.; Guimarães, T. T.; Valença, W. O.; Camara, C. A.; De Oliveira, R. N.; Da Silva, M. G.; Ferreira, V. F.; De Paiva, Y. G.; Goulart, M. O. F.; Menna-Barreto, R. F. S.; De Castro, S. L.; Da Silva Júnior, E. N. Synthesis and Anti-Trypanosoma Cruzi Activity of Naphthoquinone-Containing Triazoles: Electrochemical Studies on the Effects of the Quinoidal Moiety. *Bioorg. Med. Chem.* **2013**, *21* (21), 6337−6348.

(91) Melo, V. N.; Dantas, W. M.; Camara, C. A.; De Oliveira, R. N. Synthesis of 2,3-Unsaturated Alkynyl O-Glucosides from Tri-O-Acetyl-d-Glucal by Using Montmorillonite K-10/Iron(III) Chloride Hexahydrate with Subsequent Copper(I)-Catalyzed 1,3-Dipolar Cycloaddition. *Synth.* **2015**, *47* (22), 3529−3541.

(92) De Oliveira, R. N.; De Xavier, A. L.; Guimaraes, B. M.; Melo, V. N. E.; Valença, W. O.; Nascimento Do, W. S.; Da Costa, P. L. F.;

Camara, C. A. Combining Clays and Ultrasound Irradiation for an O-Acetylation Reaction of N-Glucopyranosyl and Other Molecules. *J. Chil. Chem. Soc.* **2014**, *59* (3), 2610−2614.

(93) Cheng, Z.; Valença, W. O.; Dias, G. G.; Scott, J.; Barth, N. D.; de Moliner, F.; Souza, G. B. P.; Mellanby, R. J.; Vendrell, M.; da Silva Júnior, E. N. Natural Product-Inspired Profluorophores for Imaging NQO1 Activity in Tumour Tissues. *Bioorg. Med. Chem.* **2019**, *27* (17), 3938−3946.

(94) Rostovtsev, V. V.; Green, L. G.; Fokin, V. V.; Sharpless, K. B. A Stepwise Huisgen Cycloaddition Process: Copper(I)-Catalyzed Regioselective "Ligation" of Azides and Terminal Alkynes. *Angew. Chemie - Int. Ed.* **2002**, *41* (14), 2596−2599.

(95) de Moliner, F.; King, A.; Dias, G. G.; de Lima, G. F.; de Simone, C. A.; da Silva Junior, E. N.; Vendrell, M. Quinone-Derived π-Extended Phenazines as New Fluorogenic Probes for Live-Cell Imaging of Lipid Droplets. *Front. Chem.* **2018**, *6* (AUG), 339.

(96) Silva, R. S. F.; De Amorim, M. B.; Pinto, M. D. C. F. R.; Emery, F. S.; Goulart, M. O. F.; Pinto, A. V. Chemoselective Oxidation of Benzophenazines by M-CPBA: N-Oxidation vs. Oxidative Cleavage. *J. Braz. Chem. Soc.* **2007**, *18* (4), 759−764.

(97) Jardim, G. A. M.; Oliveira, W. X. C.; De Freitas, R. P.; Menna-Barreto, R. F. S.; Silva, T. L.; Goulart, M. O. F.; Da Silva Júnior, E. N. Direct Sequential C-H Iodination/Organoyl-Thiolation for the Benzenoid A-Ring Modification of Quinonoid Deactivated Systems: A New Protocol for Potent Trypanocidal Quinones. *Org. Biomol. Chem.* **2018**, *16* (10), 1686−1691.

(98) Almeida, R. G.; De Carvalho, R. L.; Nunes, M. P.; Gomes, R. S.; Pedrosa, L. F.; De Simone, C. A.; Gopi, E.; Geertsen, V.; Gravel, E.; Doris, E.; Da Silva Júnior, E. N. Carbon Nanotube-Ruthenium Hybrid towards Mild Oxidation of Sulfides to Sulfones: Efficient Synthesis of Diverse Sulfonyl Compounds. *Catal. Sci. Technol.* **2019**, *9* (11), 2742−2748.

(99) Jardim, G. A. M.; Bozzi, Í. A. O.; Oliveira, W. X. C.; Mesquita-Rodrigues, C.; Menna-Barreto, R. F. S.; Kumar, R. A.; Gravel, E.; Doris, E.; Braga, A. L.; Da Silva Júnior, E. N. Copper Complexes and Carbon Nanotube-Copper Ferrite-Catalyzed Benzenoid A-Ring Selenation of Quinones: An Efficient Method for the Synthesis of Trypanocidal Agents. *New J. Chem.* **2019**, *43* (35), 13751−13763.

(100) Jardim, G. A. M.; Bower, J. F.; Da Silva Júnior, E. N. Rh-Catalyzed Reactions of 1,4-Benzoquinones with Electrophiles: C-H Iodination, Bromination, and Phenylselenation. *Org. Lett.* **2016**, *18* (18), 4454−4457.

(101) Dias, G. G.; Nascimento, T. A. d.; de Almeida, A. K. A.; Bombaça, A. C. S.; Menna-Barreto, R. F. S.; Jacob, C.; Warratz, S.; da Silva Júnior, E. N.; Ackermann, L. Ruthenium(II)-Catalyzed C−H Alkenylation of Quinones: Diversity-Oriented Strategy for Trypanocidal Compounds. *Eur. J. Org. Chem.* **2019**, *2019* (13), 2344−2353.

(102) Sunassee, S. N.; Veale, C. G. L.; Shunmoogam-Gounden, N.; Osoniyi, O.; Hendricks, D. T.; Caira, M. R.; De La Mare, J. A.; Edkins, A. L.; Pinto, A. V.; Da Silva Júnior, E. N.; Davies-Coleman, M. T. Cytotoxicity of Lapachol, β-Lapachone and Related Synthetic 1,4-Naphthoquinones against Oesophageal Cancer Cells. *Eur. J. Med. Chem.* **2013**, *62*, 98−110.

(103) Kumar, T.; Satam, N.; Namboothiri, I. N. N. Hauser−Kraus Annulation of Phthalides with Nitroalkenes for the Synthesis of Fused and Spiro Heterocycles. *Eur. J. Org. Chem.* **2016**, *2016* (20), 3316−3321.

(104) Suresh, A.; Baiju, T. V.; Kumar, T.; Namboothiri, I. N. N. Synthesis of Spiro- and Fused Heterocycles via (4 + 4) Annulation of Sulfonylphthalide with o-Hydroxystyrenyl Derivatives. *J. Org. Chem.* **2019**, *84* (6), 3158−3168.

(105) Wood, J. M.; da Silva Junior, E. N.; Bower, J. F. Rh-Catalyzed [2 + 2 + 2] Cycloadditions with Benzoquinones: De Novo Access to Naphthoquinones for Lignan and Type II Polyketide Synthesis. *Org. Lett.* **2020**, *22* (1), 265−269.

(106) Jardim, G. A. M.; da Silva Junior, E. N.; Bower, J. F. Overcoming Naphthoquinone Deactivation: Rhodium-Catalyzed C-5 Selective C-H Iodination as a Gateway to Functionalized Derivatives. *Chem. Sci.* **2016**, *7* (6), 3780−3784.

(107) Reis, W. J.; Bozzi, Í. A. O.; Ribeiro, M. F.; Halicki, P. C. B.; Ferreira, L. A.; Almeida da Silva, P. E.; Ramos, D. F.; de Simone, C. A.; da Silva Júnior, E. N. Design of Hybrid Molecules as Antimycobacterial Compounds: Synthesis of Isoniazid-Naphthoquinone Derivatives and Their Activity against Susceptible and Resistant Strains of Mycobacterium Tuberculosis. *Bioorg. Med. Chem.* **2019**, 27 (18), 4143−4150.

(108) Moura, K. C. G.; Carneiro, P. F.; Pinto, M. D. C. F. R.; Da Silva, J. A.; Malta, V. R. S.; De Simone, C. A.; Dias, G. G.; Jardim, G. A. M.; Cantos, J.; Coelho, T. S.; Da Silva, P. E. A.; Da Silva, E. N. 1,3-Azoles from Ortho-Naphthoquinones: Synthesis of Aryl Substituted Imidazoles and Oxazoles and Their Potent Activity against Mycobacterium Tuberculosis. *Bioorg. Med. Chem.* **2012**, 20 (21), 6482−6488.

(109) Dias, G. G.; Pinho, P. V. B.; Duarte, H. A.; Resende, J. M.; Rosa, A. B. B.; Correa, J. R.; Neto, B. A. D.; Da Silva Júnior, E. N. Fluorescent Oxazoles from Quinones for Bioimaging Applications. *RSC Adv.* **2016**, 6 (79), 76053−76063.

(110) Dias, G. G.; Rodrigues, B. L.; Resende, J. M.; Calado, H. D. R.; De Simone, C. A.; Silva, V. H. C.; Neto, B. A. D.; Goulart, M. O. F.; Ferreira, F. R.; Meira, A. S.; Pessoa, C.; Correa, J. R.; Da Silva Júnior, E. N. Selective Endocytic Trafficking in Live Cells with Fluorescent Naphthoxazoles and Their Boron Complexes. *Chem. Commun.* **2015**, 51 (44), 9141−9144.

(111) Grum-Tokars, V.; Ratia, K.; Begaye, A.; Baker, S. C.; Mesecar, A. D. Evaluating the 3C-like Protease Activity of SARS-Coronavirus: Recommendations for Standardized Assays for Drug Discovery. *Virus Res.* **2008**, 133 (1), 63−73.

(112) Fassio, A. V.; Shub, L.; Ponzoni, L.; Mckinley, J.; Meara, M. J. O.; Ferreira, R. S.; Keiser, M. J.; Raquel, C. Prioritizing Virtual Screening with Interpretable Interaction Fingerprints. *bioRxiv* **2022**, 1−53.

(113) Su, H.-X.; Yao, S.; Zhao, W.-F.; Li, M.-J.; Liu, J.; Shang, W.-J.; Xie, H.; Ke, C.-Q.; Hu, H.-C.; Gao, M.-N.; Yu, K.-G.; Liu, H.; Shen, J.-S.; Tang, W.; Zhang, L.-K.; Xiao, G.-F.; Ni, L.; Wang, D.-W.; Zuo, J.-P.; Jiang, H.-L.; Bai, F.; Wu, Y.; Ye, Y.; Xu, Y.-C. Anti-SARS-CoV-2 Activities in Vitro of Shuanghuanglian Preparations and Bioactive Ingredients. *Acta Pharmacol. Sin.* **2020**, 41 (9), 1167−1177.

(114) Mesecar, A. D. A Taxonomically-Driven Approach to Development of Potent, Broad-Spectrum Inhibitors of Coronavirus Main Protease Including SARS-CoV-2 (COVID-19), **2020**, to be published.

(115) Bzówka, M.; Mitusińska, K.; Raczyńska, A.; Samol, A.; Tuszyński, J. A.; Góra, A. Structural and Evolutionary Analysis Indicate That the Sars-COV-2 Mpro Is a Challenging Target for Small-Molecule Inhibitor Design. *Int. J. Mol. Sci.* **2020**, 21 (9), 3099.

(116) Kneller, D. W.; Phillips, G.; O'Neill, H. M.; Jedrzejczak, R.; Stols, L.; Langan, P.; Joachimiak, A.; Coates, L.; Kovalevsky, A. Structural Plasticity of SARS-CoV-2 3CL Mpro Active Site Cavity Revealed by Room Temperature X-Ray Crystallography. *Nat. Commun.* **2020**, 11 (1), 1−6.

(117) Douangamath, A.; Fearon, D.; Gehrtz, P.; Krojer, T.; Lukacik, P.; Owen, C. D.; Resnick, E.; Strain-Damerell, C.; Aimon, A.; Ábrányi-Balogh, P.; Brandão-Neto, J.; Carbery, A.; Davison, G.; Dias, A.; Downes, T. D.; Dunnett, L.; Fairhead, M.; Firth, J. D.; Jones, S. P.; Keeley, A.; Keserü, G. M.; Klein, H. F.; Martin, M. P.; Noble, M. E. M.; O'Brien, P.; Powell, A.; Reddi, R. N.; Skyner, R.; Snee, M.; Waring, M. J.; Wild, C.; London, N.; von Delft, F.; Walsh, M. A. Crystallographic and Electrophilic Fragment Screening of the SARS-CoV-2 Main Protease. *Nat. Commun.* **2020**, 11 (1), 1−11.

(118) Kuhn, D.; Weskamp, N.; Schmitt, S.; Hüllermeier, E.; Klebe, G. From the Similarity Analysis of Protein Cavities to the Functional Classification of Protein Families Using Cavbase. *J. Mol. Biol.* **2006**, 359 (4), 1023−1044.

(119) Franco, L. S.; Maia, R. C.; Barreiro, E. J. Identification of LASSBio-1945 as an Inhibitor of SARS-CoV-2 Main Protease (MPRO) Throughin Silicoscreening Supported by Molecular Docking and a Fragment-Based Pharmacophore Model. *RSC Med. Chem.* **2021**, 12 (1), 110−119.

(120) Gossen, J.; Albani, S.; Hanke, A.; Joseph, B. P.; Bergh, C.; Kuzikov, M.; Costanzi, E.; Manelfi, C.; Storici, P.; Gribbon, P.; Beccari, A. R.; Talarico, C.; Spyrakis, F.; Lindahl, E.; Zaliani, A.; Carloni, P.; Wade, R. C.; Musiani, F.; Kokh, D. B.; Rossetti, G. A Blueprint for High Affinity SARS-CoV-2 Mpro Inhibitors from Activity-Based Compound Library Screening Guided by Analysis of Protein Dynamics. *ACS Pharmacol. Transl. Sci.* **2021**, 4 (3), 1079−1095.

(121) Ho, B. L.; Cheng, S. C.; Shi, L.; Wang, T. Y.; Ho, K. I.; Chou, C. Y. Critical Assessment of the Important Residues Involved in the Dimerization and Catalysis of MERS Coronavirus Main Protease. *PLoS One* **2015**, 10 (12), No. e0144865.

(122) Ziebuhr, J. Molecular Biology of Severe Acute Respiratory Syndrome Coronavirus. *Curr. Opin. Microbiol.* **2004**, 7 (4), 412−419.

(123) Jukič, M.; Konc, J.; Gobec, S.; Janežič, D. Identification of Conserved Water Sites in Protein Structures for Drug Design. *J. Chem. Inf. Model.* **2017**, 57 (12), 3094−3103.

(124) Halgren, T. A.; Murphy, R. B.; Friesner, R. A.; Beard, H. S.; Frye, L. L.; Pollard, W. T.; Banks, J. L. Glide: A New Approach for Rapid, Accurate Docking and Scoring. 2. Enrichment Factors in Database Screening. *J. Med. Chem.* **2004**, 47 (7), 1750−1759.

(125) Trott, O.; Olson, A. J. AutoDock Vina: Improving the Speed and Accuracy of Docking with a New Scoring Function, Efficient Optimization, and Multithreading. *J. Comput. Chem.* **2009**, 31 (2), 455−461.

(126) Miczi, M.; Golda, M.; Kunkli, B.; Nagy, T.; Tozsér, J.; Mótyán, J. A. Identification of Host Cellular Protein Substrates of Sars-Cov-2 Main Protease. *International Journal of Molecular Sciences* **2020**, 21, 1−19.

(127) McGovern, S. L.; Helfand, B. T.; Feng, B.; Shoichet, B. K. A Specific Mechanism of Nonspecific Inhibition. *J. Med. Chem.* **2003**, 46 (20), 4265−4272.

(128) Feng, B. Y.; Shoichet, B. K. A Detergent-Based Assay for the Detection of Promiscuous Inhibitors. *Nat. Protoc.* **2006**, 1 (2), 550−553.

(129) Jadhav, A.; Ferreira, R. S.; Klumpp, C.; Mott, B. T.; Austin, C. P.; Inglese, J.; Thomas, C. J.; Maloney, D. J.; Shoichet, B. K.; Simeonov, A. Quantitative Analyses of Aggregation, Autofluorescence, and Reactivity Artifacts in a Screen for Inhibitors of a Thiol Protease. *J. Med. Chem.* **2010**, 53 (1), 37−51.

(130) McGovern, S. L.; Caselli, E.; Grigorieff, N.; Shoichet, B. K. A Common Mechanism Underlying Promiscuous Inhibitors from Virtual and High-Throughput Screening. *J. Med. Chem.* **2002**, 45 (8), 1712−1722.

(131) Boudreau, P. D.; Miller, B. W.; McCall, L. I.; Almaliti, J.; Reher, R.; Hirata, K.; Le, T.; Siqueira-Neto, J. L.; Hook, V.; Gerwick, W. H. Design of Gallinamide A Analogs as Potent Inhibitors of the Cysteine Proteases Human Cathepsin L and Trypanosoma Cruzi Cruzain. *J. Med. Chem.* **2019**, 62 (20), 9026−9044.

(132) Ma, C.; Hu, Y.; Townsend, J. A.; Lagarias, P. I.; Marty, M. T.; Kolocouris, A.; Wang, J. Ebselen, Disulfiram, Carmofur, PX-12, Tideglusib, and Shikonin Are Nonspecific Promiscuous SARS-CoV-2 Main Protease Inhibitors. *ACS Pharmacol. Transl. Sci.* **2020**, 3 (6), 1265−1277.

(133) Hilgenfeld, R. From SARS to MERS: Crystallographic Studies on Coronaviral Proteases Enable Antiviral Drug Design. *FEBS J.* **2014**, 281 (18), 4085−4096.

(134) Baell, J. B.; Holloway, G. A. New Substructure Filters for Removal of Pan Assay Interference Compounds (PAINS) from Screening Libraries and for Their Exclusion in Bioassays. *J. Med. Chem.* **2010**, 53 (7), 2719−2740.

(135) Lee, J.; Worrall, L. J.; Vuckovic, M.; Rosell, F. I.; Gentile, F.; Ton, A. T.; Caveney, N. A.; Ban, F.; Cherkasov, A.; Paetzel, M.; Strynadka, N. C. J. Crystallographic Structure of Wild-Type SARS-CoV-2 Main Protease Acyl-Enzyme Intermediate with Physiological C-Terminal Autoprocessing Site. *Nat. Commun.* **2020**, 11 (1), 1−9.

(136) Hilgenfeld, R.; Anand, K.; Mesters, J. R.; Rao, Z.; Shen, X.; Jiang, H.; Tan, J.; Verschueren, K. H. G. Structure and Dynamics of SARS Coronavirus Main Proteinase (M Pro). In *Advances in Experimental Medicine and Biology*; Springer, 2006; Vol. 581, pp 585−591. DOI: 10.1007/978-0-387-33012-9_106.

(137) Goyal, B.; Goyal, D. Targeting the Dimerization of the Main Protease of Coronaviruses: A Potential Broad-Spectrum Therapeutic Strategy. *ACS Comb. Sci.* **2020**, *22* (6), 297−305.

(138) Chen, S.; Chen, L.; Tan, J.; Chen, J.; Du, L.; Sun, T.; Shen, J.; Chen, K.; Jiang, H.; Shen, X. Severe Acute Respiratory Syndrome Coronavirus 3C-like Proteinase N Terminus Is Indispensable for Proteolytic Activity but Not for Enzyme Dimerization: Biochemical and Thermodynamic Investigation in Conjunction with Molecular Dynamics Simulations. *J. Biol. Chem.* **2005**, *280* (1), 164−173.

(139) Suárez, D.; Díaz, N. SARS-CoV-2 Main Protease: A Molecular Dynamics Study. *J. Chem. Inf. Model.* **2020**, *60*, 5815.

(140) Singh, W. M.; Baruah, J. B. Synthesis of Mixed Aryl 2,3-Diarylsulphanyl-1,4-Naphthoquinones. *Synth. Commun.* **2009**, *39* (8), 1433−1442.

(141) Qiao, J.; Li, Y. S.; Zeng, R.; Liu, F. L.; Luo, R. H.; Huang, C.; Wang, Y. F.; Zhang, J.; Quan, B.; Shen, C.; Mao, X.; Liu, X.; Sun, W.; Yang, W.; Ni, X.; Wang, K.; Xu, L.; Duan, Z. L.; Zou, Q. C.; Zhang, H. L.; Qu, W.; Long, Y. H. P.; Li, M. H.; Yang, R. C.; Liu, X.; You, J.; Zhou, Y.; Yao, R.; Li, W. P.; Liu, J. M.; Chen, P.; Liu, Y.; Lin, G. F.; Yang, X.; Zou, J.; Li, L.; Hu, Y.; Lu, G. W.; Li, W. M.; Wei, Y. Q.; Zheng, Y. T.; Lei, J.; Yang, S. SARS-CoV-2 Mpro Inhibitors with Antiviral Activity in a Transgenic Mouse Model. *Science (80-.)* **2021**, *371* (6536), 1374−1378.

(142) Sohraby, F.; Aryapour, H. Unraveling the Unbinding Pathways of SARSCoV- 2 Papain-like Proteinase Known Inhibitors by Supervised Molecular Dynamics Simulation. *PLoS One* **2021**, *16* (5), No. e0251910.

(143) Ferreira, G. M.; Pillaiyar, T.; Hirata, M. H.; Poso, A.; Kronenberger, T. Inhibitor Induced Conformational Changes in SARS-COV-2 Papain-like Protease. *Sci. Rep.* **2022**, *12* (1), 11585.

(144) Lima, D. J. B.; Almeida, R. G.; Jardim, G. A. M.; Barbosa, B. P. A.; Santos, A. C. C.; Valença, W. O.; Scheide, M. R.; Gatto, C. C.; de Carvalho, G. G. C.; Costa, P. M. S.; Pessoa, C.; Pereira, C. L. M.; Jacob, C.; Braga, A. L.; da Silva Júnior, E. N. It Takes Two to Tango: Synthesis of Cytotoxic Quinones Containing Two Redox Active Centers with Potential Antitumor Activity. *RSC Med. Chem.* **2021**, *12*, 1709.

(145) Berman, H. M.; Westbrook, J.; Feng, Z.; Gilliland, G.; Bhat, T. N.; Weissig, H.; Shindyalov, I. N.; Bourne, P. E. The Protein Data Bank. *Nucleic Acids Res.* **2000**, *28* (1), 235−242.

(146) Core R Team. *R: A Language and Environment for Statistical Computing*. R Foundation for Statistical Computing, 2018; Vol. *2*. https://www.R--project.org.

(147) Grant, B. J.; Rodrigues, A. P. C.; ElSawy, K. M.; McCammon, J. A.; Caves, L. S. D. Bio3d: An R Package for the Comparative Analysis of Protein Structures. *Bioinformatics* **2006**, *22* (21), 2695−2696.

(148) Delano, W. L. *The PyMOL Molecular Graphics System*; Delano Scientific, 2002.

(149) Zhu, K.; Borrelli, K. W.; Greenwood, J. R.; Day, T.; Abel, R.; Farid, R. S.; Harder, E. Docking Covalent Inhibitors: A Parameter Free Approach to Pose Prediction and Scoring. *J. Chem. Inf. Model.* **2014**, *54* (7), 1932−1940.

(150) Sherman, W.; Day, T.; Jacobson, M. P.; Friesner, R. A.; Farid, R. Novel Procedure for Modeling Ligand/Receptor Induced Fit Effects. *J. Med. Chem.* **2006**, *49* (2), 534−553.

(151) Bowers, K. J.; Chow, D. E.; Xu, H.; Dror, R. O.; Eastwood, M. P.; Gregersen, B. A.; Klepeis, J. L.; Kolossvary, I.; Moraes, M. A.; Sacerdoti, F. D.; Salmon, J. K.; Shan, Y.; Shaw, D. E. Scalable Algorithms for Molecular Dynamics Simulations on Commodity Clusters. *SC '06: Proceedings of the 2006 ACM/IEEE Conference on Supercomputing* **2007**, 43−43, DOI: 10.1109/sc.2006.54.

(152) Harder, E.; Damm, W.; Maple, J.; Wu, C.; Reboul, M.; Xiang, J. Y.; Wang, L.; Lupyan, D.; Dahlgren, M. K.; Knight, J. L.; Kaus, J. W.; Cerutti, D. S.; Krilov, G.; Jorgensen, W. L.; Abel, R.; Friesner, R. A. OPLS3: A Force Field Providing Broad Coverage of Drug-like Small Molecules and Proteins. *J. Chem. Theory Comput.* **2016**, *12* (1), 281−296.

(153) Ferreira, G. M.; Kronenberger, T.; Tonduru, A. K.; Hirata, R. D. C.; Hirata, M. H.; Poso, A. SARS-COV-2 Mpro Conformational Changes Induced by Covalently Bound Ligands. *J. Biomol. Struct. Dyn.* **2021**, 1−11.

(154) Jorgensen, W. L.; Chandrasekhar, J.; Madura, J. D.; Impey, R. W.; Klein, M. L. Comparison of Simple Potential Functions for Simulating Liquid Water. *J. Chem. Phys.* **1983**, *79* (2), 926−935.

(155) Darden, T.; York, D.; Pedersen, L. Particle Mesh Ewald: An N·log(N) Method for Ewald Sums in Large Systems. *J. Chem. Phys.* **1993**, *98* (12), 10089−10092.

(156) Ashhurst, A. S.; Tang, A. H.; Fajtová, P.; Yoon, M.; Aggarwal, A.; Stoye, A.; Larance, M.; Beretta, L.; Drelich, A.; Skinner, D.; Li, L.; Meek, T. D.; McKerrow, J. H.; Hook, V.; Tseng, C.-T. K.; Turville, S.; Gerwick, W. H.; O'Donoghue, A. J.; Payne, R. J. Potent in Vitro Anti-SARS-CoV-2 Activity by Gallinamide A and Analogues via Inhibition of Cathepsin L. *bioRxiv Prepr. Serv. Biol.* **2020**, *2020*, 12.23.424111.